Towards Multi-Molecular Surface-Enhanced Infrared Absorption Using Metal Plasmonics[†]

Marita Wagner,[*1,2] Andreas Seifert,[2,3] and Luis M. Liz-Marzán[*1,3,4]

Surface-enhanced infrared absorption (SEIRA) leads to a largely improved detection of polar molecules, compared to standard infrared absorption. The enhancement principle is based on localized surface plasmon resonances of the substrate, which match the frequency of molecular vibrations in the analyte of interest. Therefore, in practical terms, the SEIRA sensor needs to be tailored to each specific analyte. We review SEIRA sensors based on metal plasmonics for the detection of biomolecules such as DNA, proteins, and lipids. We further focus this review on chemical SEIRA sensors, with potential applications in quality control, as well as on the improvement in sensor geometry that led to the development of multiresonant SEIRA substrates as sensors for multiple analytes. Finally, we give an introduction into the integration of SEIRA sensors with surface-enhanced Raman scattering (SERS).

1 Introduction

Detection of molecules in different environments enables us to observe how organisms function, but also to monitor the quality of our food, air and water, among many other applications. The more molecule types we can detect simultaneously in an environment, the more wholesome our picture of said environment becomes. Most samples, especially those of biological origin, require fast, label-free, and non-invasive manipulation.

Among a wide variety of detection tools and modalities, vibrational spectroscopies probe the vibrational states of molecules, to qualitatively and quantitatively identify the presence of molecules in a mixture. The two most prominent examples of vibrational spectroscopy are infrared (IR) and Raman spectroscopy, both providing quick, label-free, and non-invasive techniques. Both IR and Raman spectroscopy probe transitions between vibrational levels, but they rely on fundamentally different physical mechanisms, namely IR absorption and Raman scattering.

In IR absorption spectroscopy, the molecule absorbs a photon corresponding to the energy of a molecular vibration, if the dipole of the molecule changes in that particular molecular vibration.[1] During an IR spectral measurement, the sample is illuminated with photons spanning the near- to far-IR energy range, to identify multiple vibrational transitions that become the molecule's vibrational fingerprint.[2] Raman scattering relies on a fundamentally different process, in which the molecule first absorbs the incoming photon (into an allowed or a forbidden state) and then scatters another photon whose energy differs from the incident photon by the energy of a molecular vibration.

In such inelastic scattering events, the photon energy can either decrease (Stokes scattering: $\omega_{in} - \omega_{vib}$) or increase (anti-Stokes scattering: $\omega_{in} + \omega_{vib}$), by the energy of the molecular vibration. For inelastic scattering to occur, i.e., for a molecule to be Raman active, the molecule must be polarizable. As a result, all molecular vibrations can be excited by the same incident laser wavelength while the outcoming photon informs about the energy of the vibrational transition.[3]

Due to the different selection rules, certain molecular vibrations are only detectable in IR or Raman spectroscopy. However, several vibrations, especially in molecules with non-center-symmetric point groups, may be observed by both techniques.[4] Furthermore, most compounds contain IR and Raman active molecular vibrations, such as mercaptobenzonitrile (MBN). Therefore, both IR and Raman spectroscopy can inform us about the fingerprint region with characteristic vibrational lines of molecules. However, in the analysis of aqueous samples Raman is often at an advantage, because water has strong IR absorption bands, but is only a weak Raman scatterer.[5]

A relevant requirement for monitoring biological and environmental samples is the possibility of detecting trace amounts. However, IR absorption (10^{-20} cm^2 per molecule) and Raman scattering (10^{-29} cm^2 per molecule) cross-sections are small and, as a result, when studying samples at very low concentrations the recorded signals are often too weak. In this context, research has been carried out to enhance the signal that can be recorded by both IR and Raman spectroscopy, largely in the context of plasmon resonances. Plasmons are collective oscillations of conduction-band electrons in metals,[6,7] which lead to charge density waves, either inside a metal (bulk plasmons) or at a metal-dielectric interface (surface plasmon polaritons).[8]

In nanoparticles, the spatial confinement leads to the formation of so-called localized surface plasmon resonances (LSPR).[8,9] Surface plasmon polaritons and LSPR result in a local magnification of electromagnetic fields.[10] Such a magnification of the electromagnetic field in turn leads to an enhancement of IR and Ra-

[1] CIC biomaGUNE, Basque Research and Technology Alliance (BRTA), Paseo de Miramón 194, 20014 Donostia-San Sebastián, Spain. E-mail: mwagner@cicbiomagune.es; llizmarzan@cicbiomagune.es

[2] CIC nanoGUNE, Basque Research and Technology Alliance (BRTA), 20018 Donostia-San Sebastián, Spain.

[3] IKERBASQUE, Basque Foundation for Science, 43009 Bilbao, Spain.

[4] Centro de Investigación Biomédica en Red, Bioingeniería, Biomateriales y Nanomedicina (CIBER-BBN), 20014 Donostia-San Sebastián, Spain.

man signals from molecules that are placed nearby the plasmonic surface, resulting in a process broadly termed surface-enhanced spectroscopy.[11,12] Although surface-enhanced infrared absorption (SEIRA) and surface-enhanced Raman scattering (SERS) were discovered around the same time, the larger enhancement factors achieved in SERS have made it significantly more popular.

In 1980, Hartstein and colleagues discovered SEIRA by placing analyte monolayers on top of colloidal silver films, which led to a signal enhancement of a factor 20.[13] Albeit only a few years after the discovery[14] and identification[15,16] of the SERS effect, at that time SERS signal enhancements factors had already reached 10^6.[17] In 1997, SERS first reached single molecule detection, with enhancement factors of 10^{10} to 10^{14},[18,19] whereas 20 years later the furthest milestones in SEIRA enhancement factors lie at 10^7.[20–22] This review focuses on recent advances of the less popular SEIRA, as a sensing tool for biological and chemical samples. We focus on the design of metal-plasmonic substrates for the detection of one or multiple analytes, to ultimately provide our own insights into the potential combination of SEIRA and SERS.

IR absorption occurs over a wide wavelength range and depends on the energy of the molecular vibrations. Therefore, the appropriate plasmon resonance of the metallic structure should lie at, or close to, the energy of the molecular vibration to be enhanced.[23,24] Substrates may be designed to enhance specific molecular vibrations in a mixture (for example proteins, fatty acids or environmental toxins), leading to the selective enhancement of a compound over others.[20,25–29]

Furthermore, since SEIRA solely probes the sample close to the surface, the IR water absorption peak can be suppressed.[5] Recent advances in pattern design of metallic SEIRA substrates have seen the emergence of multi-resonant substrates, which can enhance multiple sections of the IR range, thereby allowing for the detection of multiple analytes.[30–32] Since for SERS the plasmonic frequency should closely match the excitation laser line,[8,33–35] combined SEIRA and SERS consequently asks for multi-resonant substrates supporting plasmons at the wavelength of all IR peaks to be enhanced, as well as plasmons closely matching the Raman excitation laser beam.[36–45]

2 Background

Light irradiation of metal nanostructures generates confined electromagnetic near-fields, which are essential for the enhancement of IR signals. Such near-field enhancements originate from the collective electronic oscillations within the nanostructure, i.e., the LSPR. Therefore, these nanostructures become antennas for light, and their size, shape and material define their electromagnetic properties. One of the simplest antennas, linear nanorods, function as half-wave dipole antennas, which produce plasmon resonances whose wavelengths depend mainly on the rod length L.

The main LSPR of such antennas originates from dipolar modes within the whole antenna, with one dipole corresponding to the length of the antenna, thus being referred to as the longitudinal mode, and another originating from the width of the antenna, the so-called transversal LSPR mode.[46,47] Each of these modes may be excited selectively by tuning the polarization of light.[41]

In addition to this main dipolar resonances, others (higher order multipoles) may also occur in nanorod antennas, but we chose not to elaborate on these here.[48] Half-wave dipole nanoantennas can be used to generate LSPR in the IR. The relationship between the antenna length (width in case of transversal modes) and the resonance frequency has been derived by Novotny as:[49]
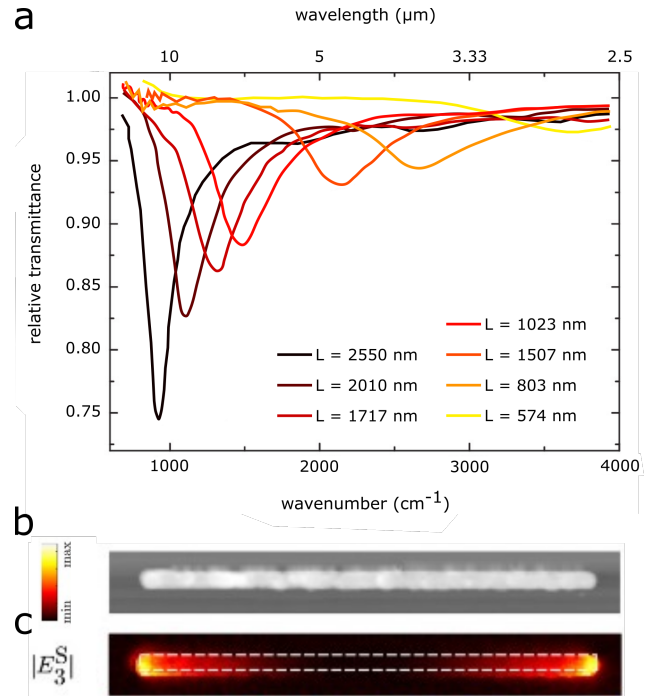

Fig. 1 (a) Experimental relative transmittance of rod-antennas of different lengths with constant width (58 nm) and height (60 nm). Adapted from ref. 50 with permission from AIP Publishing. (b) SEM image of a rod-antenna and (c) its near-field enhancement distribution, as measured with scattering-type scanning near-field optical microscopy (s-SNOM), with polarization direction along the antenna (parallel). Adapted from ref. 51 with permission from John Wiley and Sons.

$$\lambda = \frac{2L}{m}na_1 + a_2, \qquad (1)$$

where λ is the wavelength of the mode, m the mode number (a positive integer), and n the refractive index of the surrounding medium.[46] The parameters a_1 and a_2 originate from the antenna geometry and the phase associated with reflections at the antenna end. An increase of the refractive index around the nanoantenna evokes a redshift of the resonance, which has been applied for sensing based on refractive index changes occurring upon binding of analytes.[12] The main factor determining the central plasmon resonance frequency in IR rod-antennas is their length, as illustrated in Figure 1a.[52] The aspect ratio, included into parameter a_1, additionally influences the antenna resonance; a smaller aspect ratio (wider antenna of the same length) displays a broader and blueshifted resonance.[52,53] More complex antenna designs often comprise combinations of linear rods and, as a result, the LSPR becomes a combination of the corresponding resonances of linear antennas.[20,31,54,55]

For the main dipolar mode, the highest near-field enhancements are found at the antenna tips, as shown in Figure 1c. In

addition to the near-field enhancements of individual antennas, additional enhancements may also stem from the arrangement of multiple antennas into regular arrays (Figure 2a). The strength of the LSPR of a single antenna depends on the incident electric field. Antennas in periodic arrays may also feel the electric field generated by the dipoles of the other antennas in the array, thus generating a stronger near-field in each individual antenna (Figure 2b). [23,56–58] The intensity of this collective enhancement depends on the substrate, the spacing between the antennas, and the wavelength and angle of the incident light. The near-field intensity is highest when the dipolar modes of the antennas in the array are approximately in phase. [57]
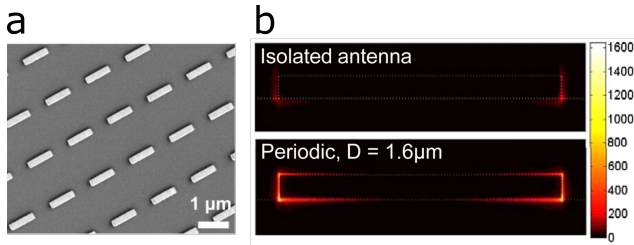

Fig. 2 (a) SEM image of a rod-antenna array. (b) Cross-sectional distribution of the near-field intensity of an isolated antenna and an antenna in a periodic array. Reproduced with permission from ref. 57. Copyright 2009 National Academy of Sciences.

2.1 Fano Resonances

The peak of a surface-enhanced molecular vibration does not appear as an individual peak in the spectrum, but rather as a modulation in the plasmonic line-shape. The plasmon resonance can be described by a Lorentzian line profile, analogous to that of a harmonic oscillator. The molecular vibration thus shows up on top of the LSPR´s Lorentzian line-shape as an asymmetric modulation of the profile. The asymmetric profile of the molecular vibration can be described by a so-called Fano resonance. Fano resonances were first described in 1961 by Ugo Fano, in his quantum mechanical description of auto-ionized states of atoms, which have a characteristic asymmetry in their line-shape. [59] Fano described the asymmetric line-shape as:

$$I \propto \frac{(F\gamma + \omega - \omega_0)^2}{(\omega - \omega_0)^2 + \gamma^2}, \qquad (2)$$

where I is the intensity, F the Fano parameter describing the degree of asymmetry, and γ the width of the resonance with frequency ω_0. The asymmetry originates from constructive and destructive interference, which in the case of SEIRA occurs between the broadband plasmon resonance and the narrowband molecular vibration. [60,61] Using highly engineered SEIRA substrates (so-called metamaterials), Fano line-shapes may also be observed, with no relation to the surface enhancement effect. Different plasmon modes within various components of a metamaterial geometry may interact with each other and give rise to plasmon modes, which are also described by the Fano line-shape. [30,62]

2.2 Coupled Harmonic Oscillator Model

The interaction of the LSPR with a molecular vibration can be intuitively understood as a coupled harmonic oscillator. [12,60,61] In this classical analogy to the Fano formalism, the LSPR couples to the molecular vibration as depicted in Figure 3b. The IR illumination excites the plasmon resonance of the antenna, which acts as a "bright" mode. For the molecular vibration, with a low absorption cross section, the far-field IR illumination only minimally excites the molecular vibration, this mode is thus referred to as "dark". The coupling between the "bright" plasmon mode and the "dark" molecular vibration makes the molecular vibration visible as a modulation on top of the simple harmonic oscillator mode of the plasmon resonance. [12,63] On a more intuitive basis, the plasmon resonance can be understood as transferring its energy to the molecular vibration, so that the intensity of the LSPR decreases at the energy of the molecular vibration.
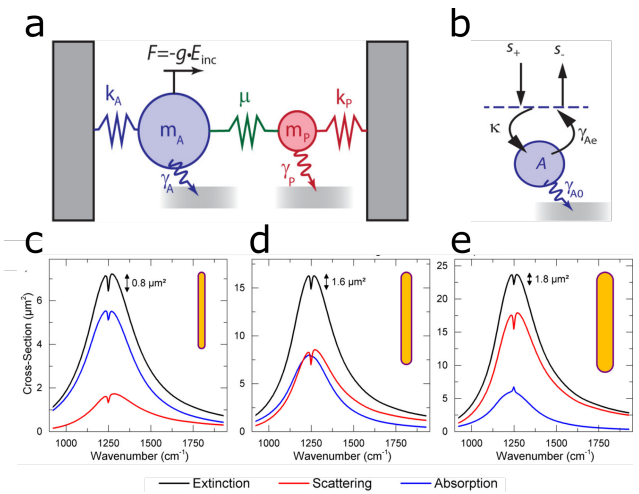

Fig. 3 (a) Schematic view of a damped harmonic oscillator consisting of a bright (A) and a dark (P) mode. The external radiation drives the bright mode A via a force $g*E_{inc}$. The dark mode P does not interact with the external field but is indirectly driven by coupling with mode A via a driving rate, μ. The bright mode A experiences a larger damping, γ_A, than the dark mode, γ_P. (b) Schematic illustration of a cavity in the temporal coupled mode theory. Reprinted with permission from ref. 64. Copyright 2013 American Chemical Society. (c) Extinction (black), absorption (blue), and scattering (red) of a dominantly absorbing antenna enhancing the IR signal (d) of a critically coupled antenna (scattering and absorption approximately equal) and (e) of a dominantly scattering antenna enhancing signal. Adapted with permission from ref. 53. Copyright 2015 American Chemical Society.

2.3 Temporal Coupled Mode Theory

The coupling of the plasmon to the molecular vibration can be explained by the harmonic oscillator model. However, an important aspect is given by the interactions described by the temporal coupled mode theory (TCMT). [65–67] This theory offers additional insight into the Fano interaction between the plasmon resonance and the molecular vibration. [63] TCMT describes how an intrinsic absorption by the material and external radiation losses change the molecular vibration and its line-shape in the SEIRA spectrum. More specifically, the TCMT describes the response of a single cav-

ity to an incoming and outgoing travelling wave (s_+ and s_-), via the following equations:[5]

$$\frac{dA}{dt} = j\omega_\text{A}A - (\gamma_\text{A0} + \gamma_\text{Ae})A + \kappa s_+ \qquad (3)$$

$$s_- = -s_+ + \kappa A. \qquad (4)$$

Equation 3 formulates the time evolution of the resonance amplitude A of the cavity (plasmon), whereas Equation 4 describes the propagation of travelling waves. The mode frequency is ω_A and the sum of losses is given by γ, with γ_A0 being intrinsic material losses and γ_Ae describing radiative losses into the far-field.

The input traveling wave (s_+) is coupled to the resonant mode via the fraction κ (Equation 4), as illustrated in Figure 3b. The output travelling wave (s_-) is defined via Equation 4 and depends on the scattering of the system, contained in γ_Ae. The coupling term κA describes the degree of damping on the plasmon resonance, which in turn changes the ratio between external and internal losses in the coupled system. Such differences in damping rates lead to different line-shapes in the spectrum, which can be understood by examining the ratios of losses of the system (Figure 3c-e).[64]

We start by examining the loss of the bright mode, i.e., the plasmon resonance. The loss of the bright mode contains contributions from both scattering and absorption. Scattering accounts for a radiative loss and is formally explained by the radiative damping rate γ_Ae. Absorption, also referred to as intrinsic loss, is contained in the intrinsic damping constant γ_A0. The ratio $\gamma_\text{Ae}/\gamma_\text{A0}$ (radiative loss divided by intrinsic loss) determines the line-shape when the plasmon resonance (LSPR) enhances the molecular vibration. When the ratio is smaller than 1 ($\gamma_\text{Ae}/\gamma_\text{A0} < 1$), absorption dominates and the system is referred to as undercoupled. In an undercoupled system, the molecular vibration appears as a dip (lower intensity than the plasmon), as shown in Figure 3c.[53,64,67]

On the other hand, when the ratio is larger than 1 ($\gamma_\text{Ae}/\gamma_\text{A0} > 1$), scattering dominates and the system is referred to as overcoupled. In an overcoupled system the molecular vibration appears at a higher intensity than the plasmon band, as shown in Figure 3e.[53,64,67]

By including the effect of coupling to the dark mode P via the coupling constant μ, the system also includes the damping constant of the molecular vibration γ_p. The system is undercoupled if $\gamma_\text{Ae}/(\gamma_\text{A0} + \gamma_\text{p}) < 1$ and overcoupled if $\gamma_\text{Ae}/(\gamma_\text{A0} + \gamma_\text{p}) > 1$. In the case that $\gamma_\text{Ae}/(\gamma_\text{A0} + \gamma_\text{p}) = 1$, the system is referred to as critically coupled. If the system is critically coupled, in addition to the molecular vibration having the same frequency as the plasmon, no signal is detected (Figure 3d, blue line). When the bright plasmonic mode couples to the dark molecular vibration, the mode amplitude also includes the effective damping constant $\gamma_\mu = \mu^2\gamma_\text{p}/[(\omega - \omega_\text{p})^2 + \gamma_\text{p}^2]$ and the effective frequency shift $\omega_\mu = \mu^2(\omega - \omega_\text{p})/[(\omega - \omega_\text{p})^2 + \gamma_\text{p}^2]$, to yield the mode amplitude of the plasmonic mode, assuming a time harmonic field[64,67]

$$j\omega A = j\omega_\text{A}A - (\gamma_\text{A0} + \gamma_\text{Ae})A - \gamma_\mu A + j\omega_\mu A + \kappa s_+. \qquad (5)$$

2.4 Enhancement Factor

The quality of enhancement of a SEIRA substrate is usually expressed as the enhancement factor (EF).[41,68] The EF compares the signal strength of the enhanced signal and that of the equivalent unenhanced signal through:

$$EF = \frac{I_\text{SEIRA}}{I_0}\frac{A_0}{A_\text{SEIRA}}, \qquad (6)$$

where I_SEIRA is the enhanced signal strength, I_0 the unenhanced signal strength, A_SEIRA denotes the area (volume) covered (filled) by analyte molecules in the SEIRA measurement, and A_0 the area covered by analyte molecules in the reference measurement. Since the largest field enhancement is usually found at the tip end of the antenna, the area of such tip-ends is often used as an approximation.[41]

3 Biological Sensing

Biological sensing, or biosensing, refers to the detection of molecules of biological origin, such as proteins or lipids, in an isolated state or within their natural environment. The characteristic vibrational modes of (bio-)molecules make possible their identification via IR spectroscopy.[69,70] In developing SEIRA-based biosensors, one has to consider two aspects: the SEIRA biosensor must enhance the vibrations of interest and capture the analytes close to the enhancing surface. The vibrational modes of biomolecules span a band width of $7\,\mu$m as illustrated in Figure 4, ranging from lipids at $3\,\mu$m ($3333\,\text{cm}^{-1}$),[32,69] proteins (amide I and amide II band) at $6\,\mu$m ($1666\,\text{cm}^{-1}$),[28,69,71] lipids at $3\,\mu$m ($3333\,\text{cm}^{-1}$),[32,69] nucleic acids and carbohydrates at $10\,\mu$m ($1000\,\text{cm}^{-1}$).[55] Promising SEIRA-based biosensors have been constructed not only from metals, but also from van der Waals (e.g., graphene[72,73]) and dielectric materials (e.g., semiconductors[74]). In this section, we discuss the use of metallic SEIRA substrates for sensing of DNA, protein secondary structure, biochemical processes of membranes, and measurements of whole cells. We have grouped references by the targeted biomolecule, mainly distinguished by the target vibration to be detected. However, the surface functionalization responsible to bind the targeted biomolecule close to the plasmonic surface also plays an important role.
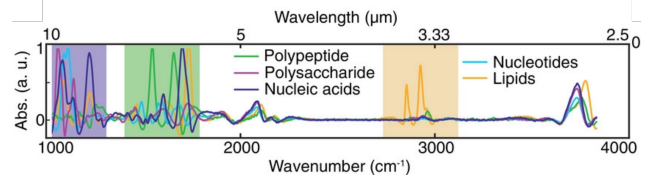

Fig. 4 IR absorption spectra of representative species of all major types of biomolecules. Reproduced under the Creative Commons Attribution License (CC BY-NC-ND 4.0) from ref. 55 with permission from John Wiley and Sons Publishing.

3.1 DNA and RNA

SEIRA has been used to detect DNA, both qualitatively[75] and quantitatively[20]. To do so, the majority of SEIRA-based DNA

sensors utilize functionalized surfaces, which bind a specific DNA sequence only. However, examples exist where e.g. a point mutation was differentiated from the wild type, based on their respective spectral signatures.[75] Synthesized gold nanoparticles covered with a layer of the analyte gene were assembled into thin films on a glass slide, where the formation of nanoparticle clusters resulted in the enhancement of the IR signal of DNA. In this manner, detection of the point mutation adenosine to guanine in the human TGFBI (transforming growth factor beta-induced) gene was enabled with 50 % higher efficacy than in conventional FTIR analysis. However, the authors did not specify which plasmonic vibration was responsible for enhancing the DNA signal. On the other hand, an example for using a DNA recognition sequence such as for the rapid detection of SARS-CoV-2 genomic sequences[76]. Gold was evaporated on a substrate, resulting in the formation of random gold clusters supporting plasmon resonances at various wavelengths. The surface was functionalized with single-stranded DNA, which could recognize SARS-CoV-2 specific genomic sequences. The substrate enhanced the absorption peaks of the DNA-base, from 1500 to 1720 cm^{-1} (C=O and C=N stretching). Upon hydrogen bonding of the two strands, these vibrations would change due to the different chemical environment. With the help of principal component analysis (PCA), the spectral response of SARS-CoV-2 sequences could be differentiated from other genomic sequences. In combination with a fast genomic multiplication technique, the method was able to detect concentrations of 5 aM within 30 minutes. SEIRA substrates for the detection of other viruses were recently reviewed.[77]
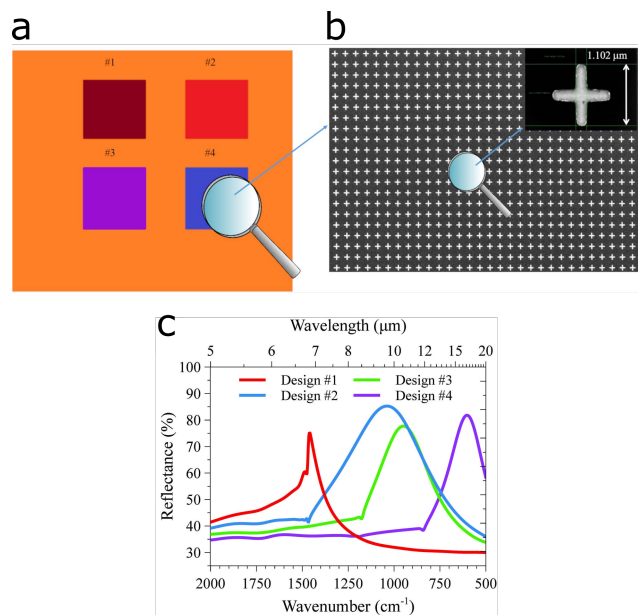
Fig. 5 DNA detection using a pixelated SEIRA substrate. (a) Pixelated substrate with four patterned designs. (b) SEM micrographs of the surface and (inset) with detail on the length of the cross and the period of the unit cell. (c) Numerically computed reflectance spectra of the four designs in the pixels. Adapted from ref. 20 under the Creative Commons Attribution License (CC BY). Copyright 2021 Di Meo, Moccia, Sanità, Crescitelli, Lamberti, Galdi, Rendina and Esposito.

A more systematic approach was used to selectively target the

C=O stretching vibration of microRNA *miRNA-155*, a biomarker for cancer, at 1665 cm^{-1}, using gold disc antennas that support a plasmon mode at this energy.[78] The sensor utilized tetrahedral DNA structures as the capturing mechanism for mircoRNA, leading to a limit of detection of 100 fM. A more elaborate protocol was devised to identify the most suitable antenna length, by means of a pixelated substrate, to lower the limit of detection for DNA.[20] The design involved multiple plasmon wavelengths on a single sensor, specifically four pixels contained cross-shaped antennas of four different antenna lengths (Figure 5c), which were functionalized with a recognition layer binding a specific DNA sequence only. The two best performing pixels reached EFs of 7×10^6 and 2.3×10^6, thereby lowering the limit of detection down to 50 fM. The same group used a similar pixelated sensor to detect vitamin D via the corresponding functional group and fingerprint region in the same substrate[79]
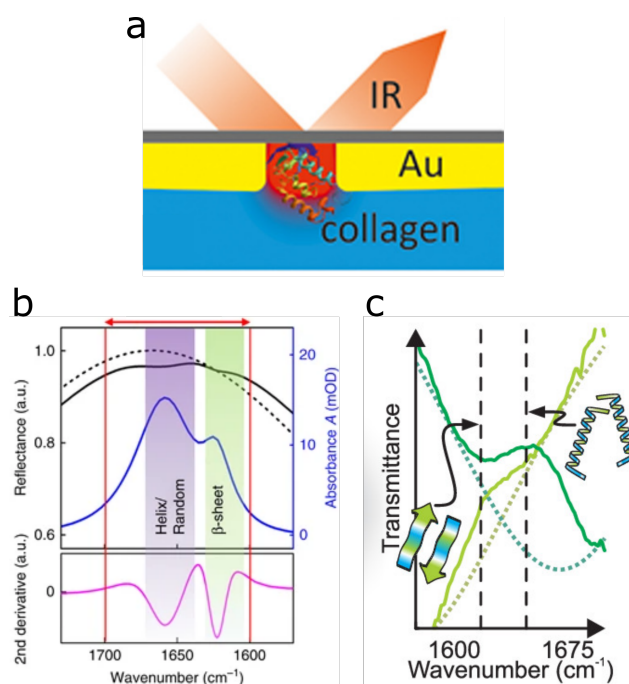
Fig. 6 (a) Graphical interpretation of nanoslits (red) used in reflection IR geometry, containing collagen molecules. Adapted with permission from ref. 28. Copyright 2019 American Chemical Society. (b) The amide I band of proteins as marked with the red arrow, indicating the spectral range of α-helix and random configurations at 1650 cm^{-1} and the β-sheet configuration peak closer to 1600 cm^{-1} and the corresponding second derivative for analysis. Reproduced under the Creative Commons License (CC BY-NC-ND 4.0) from ref. 71 with permission from Springer Nature. (c) Secondary protein structure of poly-*L*-lysine, as investigated with ultrashort IR pulses. Dark green depicts the β-sheet configuration in D$_2$O solution; light green corresponds to the structure when the denaturing agent SDS is present. The dotted line is the bare antenna resonance. Reprinted with permission from ref. 80. Copyright 2019 American Chemical Society.

3.2 Proteins

The secondary structure or folding of proteins is governed by intramolecular and intermolecular hydrogen bonding. This structure is of high relevance because protein misfolding may result in

diseases such as Parkinson's, type two diabetes, and Alzheimer´s, among others.[81]

The amide I band of proteins ($1700\,\mathrm{cm^{-1}}$ to $1600\,\mathrm{cm^{-1}}$) contains contributions from the C=O and C−N vibrations in peptide bonds, which vary with protein folding, and can be analysed by the second derivative of the IR signal (Figure 6b).[82] By engineering the size of nanoantennas to exhibit a plasmon resonance in the amide I band region, the secondary structure of minute protein amounts could be elucidated using nanoslits,[28] evaporated gold clusters,[29] and rod-shaped antennas.[71,80,83,84]

The spectral line of the amide I band of proteins overlaps with the water absorption band.[5] Therefore, for measurements of proteins in aqueous environment the water absorption band should be suppressed. In fact, also SEIRA measurements of other aqueous samples benefit from such measurements in reflection geometry, because water often absorbs and distorts the signal.

Adato and Altug introduced a solution by performing SEIRA measurements in IR reflection, illuminating from the back through an IR transparent CaF_2 window, as illustrated in Figure 6a.[5] The setup only collects signal from the plasmonic interface and avoids traversing the bulk of water above, thereby immensely reducing the IR absorption band of water. Most studies performed in aqueous environment currently employ a similar setup, to reduce distortions of the recorded signal originating from water absorption.[30,32,85]

Applications of this setup include the differentiation of random coil conformations from β-sheet structures in α-synuclein protein monolayers, as well as native β-sheet from pathological β-sheet conformations of streptavidin in water at static conditions (without movement of the medium).[71] Building upon these findings, the same group monitored the reversible denaturation of β-sheet configurations in α-synuclein monolayers in real time using a flow cell.[84]

It is well known that the largest field enhancement of plasmonic rod-like antennas is localized at their tips[12] and can be further increased by reducing the tip-to-tip spacing between the antennas. Indeed, by reducing the spacing between antennas below a hundredth of the excitation wavelength, nanogaps are obtained, that can generate large field enhancements.[21,86] By coupling the already intensified enhancement from the nanogaps to far-field enhancements stemming from the distance between the antenna rows, limits of detection for streptavidin molecules were reported as low as two proteins per gap in dry conditions, $100\,\mathrm{pg\,mL^{-1}}$ in aqueous media.[87] In addition to detecting the protein at low concentrations, the limit of detection for the determination of the secondary protein structure in aqueous media was $500\,\mathrm{ng\,mL^{-1}}$. Along similar lines, the lower limit of detection of the streptadivin-biotin interaction was 10^{-10} M, measured on Au-Ag semi-nanoshells,[88] and 10^{-12} M on colloidal gold nanobipyramids.[89] Giessen, Neubrech and colleagues studied the reversible transformation between α-helix and β-sheet for poly-L-lysine, using rod-shaped nanoantennas to enhance the amide I band.[83] By coupling the poly-L-lysine monolayer to the plasmonic rod-antennas, the reversibility of the changes was demonstrated *in vitro*. An immobilization protocol has also been developed to study large transport proteins with SEIRA, which should enable analysis of a wider range of biochemical processes.[90]

The inverse structure of rod-shaped antennas, linear nanoslits, display the same plasmon resonance as their rod-shaped counterparts, but the near-field enhancement is situated inside the slits.[91] By placing collagen-like molecules directly into the nanoslit, enhancements larger than those with equivalent setups based on antennas were achieved, and served to elucidate reversible changes from native (triple helix) to unfolded collagen structures (Figure 6a).[28] A similar setup by the same group using rod-shaped nanoslits instead of antennas (inverse structure) enhanced yet again the amide I band, likewise visualizing reversible changes of protein structure. An advantage of using slits over antennas is that the sensor surface is almost completely covered by gold, making it conductive and available for studying electrochemical interactions of the sample, in conjunction with SEIRA.[92]

A benchmark towards lower limits of detection is provided by the observation of α-helix to β-sheet conformational changes in poly-L-lysine, in attomolar concentrations and attomolar volumes, on single gold antennas.[80] The measurement was enabled by an ultrashort pulsed IR laser source, which, due to the short pulse duration, is spectrally extremely broad (laser width $125\,\mathrm{cm^{-1}}$) and could simultaneously excite the resonances of α-helix at $1648\,\mathrm{cm^{-1}}$ and β-sheet at $1618\,\mathrm{cm^{-1}}$. The laser was used in conjunction with rod-shaped antennas featuring plasmon resonances within the same spectral window. Under D_2O solution, poly-L-lysine appears in both α-helix and β-sheet configurations, but upon injection of sodium dodecylsulfate (SDS), it denatures into a β-sheet configuration (Figure 6c). The measurements were verified with synchrotron measurements, which offer IR light of high brilliance, but are expensive and have limited availability.[93–95] The results using the pulsed laser aligned with the verification by synchrotron light, but can be performed significantly faster.

Changes in protein folding are a frequent concomitant of molecular binding events.[96] The binding of the anticancer drug Lapatinib to the kinase domain of the epidermal growth factor (EGFR) resulted in structural changes of the latter, which could be monitored by SEIRA. As the long axis of the rod-antenna should match the polarization of the IR light source, cross-aligned rod antennas would provide a plasmon resonance with the orientation of each arm. By using a crossed geometry with equal antenna lengths, the amide I and amide II vibrations could be excited regardless of the polarization. This polarization-independent SEIRA substrate was used to detect signal reductions of 2% for α-helix and 1% for β-sheet , which indicated a binding of the drug to the EGFR domain.[85]

Besides well-defined geometries, such as rod-antennas and slits, random gold clusters, usually formed by evaporation of gold onto substrates, display plasmon resonances in the amide I and amide II spectral regions. Apart from the gold cluster size, which is governed by the evaporation time, also the immobilization procedure used for binding the proteins to the plasmonic surface affected the EF of the protein monolayer.[29]

Gold can also be directly evaporated onto a crystal used in attenuated total internal reflection (ATR) IR spectroscopy, which requires minimal to no sample preparation. Wang and colleagues

reviewed the use of SEIRA in such ATR-IR setups.[36]

3.3 Lipid Membranes

The cellular membrane plays a key role in cell signalling and regulates the interaction of cells with external components, such as drugs and pathogens.[97] The Haltug group developed multiresonant substrates and advanced data analysis strategies for the real-time monitoring of biochemical processes involving the lipid membrane.[32,55,69] The substrates used in the three aforementioned studies increase in complexity to enable analysis of ever more components in the sample. The first study utilizes two separate antenna arrays of different antenna sizes on the same substrate (Figure 7a).[69] In the second study, both antenna sizes were combined into the same array, enabling the analysis of two analytes at the same location (Figure 7b,c).[32] In the third study, two separate antenna arrays, one of which containing two antenna sizes, a total of three antenna sizes were built into a single substrate (Figure 7d).[55] The multiresonant substrates enhance the signal of the different components involved in such interactions. The vibrations of lipids allow monitoring the integrity of the lipid bilayer and the additional plasmon resonances enable monitoring of proteins and other components within the membrane.

In the first study, a biomimetic membrane emulating the lipid bilayer was assembled on a substrate with two antenna arrays (Figure 7a).[69] One antenna array comprised rod-shaped antennas, which enhanced the lipid-indicative methylene doublet (CH_2 and CH_3 at $2850\,cm^{-1}$ and $2930\,cm^{-1}$), whereas the second antenna array served to monitor proteins via the amide I and II bands ($1560\,cm^{-1}$ and $1660\,cm^{-1}$). The sensor resolved the assembly of the biomimetic membrane onto the antennas and the subsequent formation of a protein monolayer atop the membrane.

Two years later, the same group combined both antenna sizes into the same array, enhancing the lipid and protein signals in the same location, as illustrated in Figure 7b, c.[32] The substrate was used to monitor the signal of GABA (a neurotransmitter - protein) released from vesicles (lipid membrane), caused by the injection of membrane-rupturing melittin (a protein). The mechanism follows the same scheme depicted in Figure 8a, with only one type of cargo and one melittin injection. With the help of multiple linear regression analysis, the signal from all three components could be discerned.

Building on these findings, a single resonant nanogap array introduced in ref. 87 providing a resonance at $1600\,cm^{-1}$ and a novel dual-resonant nanogap array with resonances at $1200\,cm^{-1}$ and $2900\,cm^{-1}$ were combined into one biosensor (Figure 7d)[55]. With these three resonances in one substrate and deep learning-augmented data analysis, the signal of all major classes of biomolecules, i.e., carbohydrates, lipids, nucleotides, and proteins could be acquired. The substrate captured vesicles (lipid bilayers) carrying nucleotides and sucrose. Injected melittin ruptured the lipid bilayer of the vesicles, thereby releasing the contained nucelotides and sucrose, as illustrated in Figure 8a. By analysing the spectral data with multilinear regression and with the assistance of a deep neural network, the nucleotide, sucrose, lipid and melittin signals could be isolated (Figure 8b).
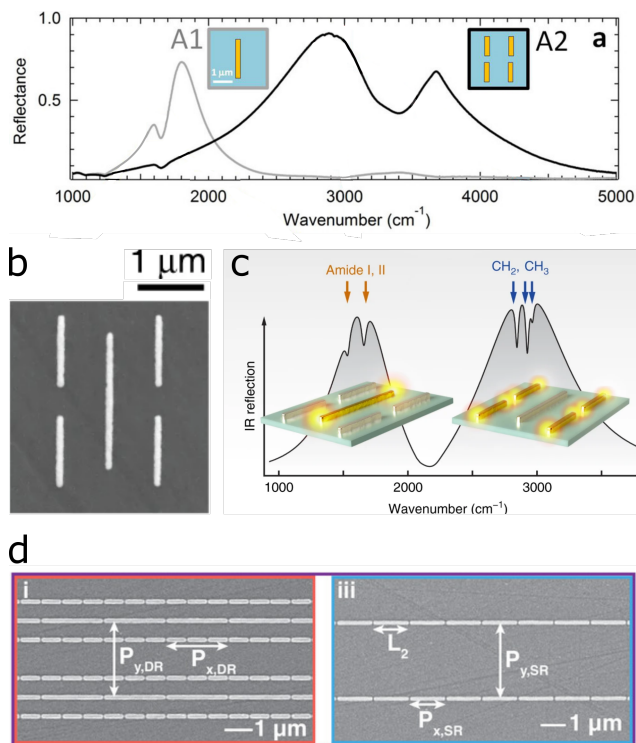

Fig. 7 (a) Two separate antenna arrays on the same sensor to separately enhance lipid and protein fingerprints. Adapted with permission from ref. 69. Copyright 2016 American Chemical Society. (b) Combination of two antenna arrays into one self-similar array for enhancement of lipid and protein fingerprints in the same array. (c) Plasmon resonances enhance the amide I and II bands ($1560\,cm^{-1}$ and $1660\,cm^{-1}$) and lipid-indicative methylene doublet (CH_2 and CH_3 at $2850\,cm^{-1}$ and $2930\,cm^{-1}$, respectively). Reproduced under the Creative Commons Attribution Licence (CC BY 4.0) 32 with permission from Springer Nature. (d) Two separate nanogap antenna arrays for the enhancement of proteins, lipids, nucleic acids and carbohydrates. One array combines two antenna sizes, whereas the other comprises a single antenna size. Reproduced under the Creative Commons Attribution License (CC BY-NC-ND 4.0) from ref. 55 with permission from John Wiley and Sons Publishing.
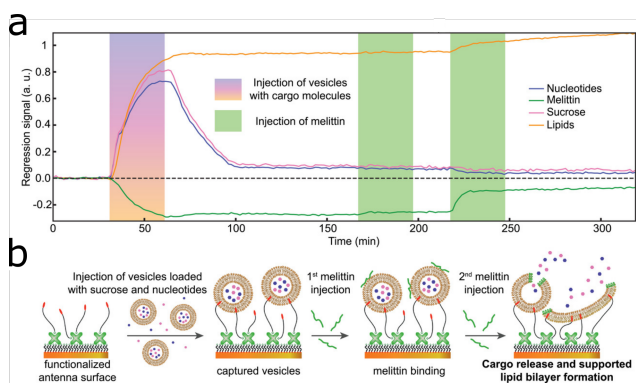

Fig. 8 (a) Scheme of the capture of a cargo-filled vesicle by a functionalized antenna array and two melittin injections with cargo release. (b) Deep learning-augmented data analysis of spectral loadings gives separated nucleotide, melittin, sucrose and lipid signals. Reproduced under the Creative Commons Attribution License (CC BY-NC-ND 4.0) from ref. 55 with permission from John Wiley and Sons Publishing.

3.4 Live Cells

Research on cells is one of the most important tools at hand, toward understanding organisms and disease, as well as to develop suitable treatments. SEIRA has been proposed as a suitable tool for the classification of pathogens. Columnar gold nanorod arrays displaying broad plasmon resonances in the IR provided qualitative differentiation of three bacterial species (*E. coli*, *S. aureus*, and *B. subtilis*). With the aid of both unsupervised and supervised machine learning techniques, quantitative information about the bacterial content in the sample was obtained.[98]

A similar experiment was conducted with the bacterial species *C.albicans*, *E.coli*, and *S.aureus*, by mixing the bacterial suspensions with silver nanoparticles.[99] Although silver nanoparticles displayed maximum absorbance at 420 nm ($23\,841\,\mathrm{cm}^{-1}$), SEIRA enhancement appeared to be provided for the whole IR range, the origin of which is insufficiently explained by the report, as the plasmonic response was only measured from the UV and up to 800 nm. SEIRA measurements, as well as conventional FTIR measurements without silver nanoparticles, were performed in ATR geometry and the data was analysed with PCA, which aided the distinction among different species. Data analysis with PCA shows a clearer separation of the bacterial species in SEIRA than that obtained with FTIR, thus leading to an improved classification protocol. Unfortunately, quantification of this improvement was not provided by the authors. An interesting aspect in this work was the ability of the bacteria–silver nanoparticle mixture, to provide enhancements also for SERS. Again with the aid of PCA, SERS measurements also allowed to differentiate between the various bacterial species. SEIRA has also been used to detect the SARS-CoV-2 virus, both in gas and liquid, and clinical samples could be analysed for rapid detection.[100]

Besides detection of pathogens, SEIRA has also been used to monitor biochemical processes in whole mammalian live cells.[30,101,102] In an interesting example, temporal changes of membrane permeability induced by ultrasound were studied through the rate of internalization of gold nanospheres into fibroblast cells. The gold nanospheres were previously covered with the SEIRA marker 4-aminothiophenol to give a SEIRA signal. The quantity of the nanosphere–marker complex directly reflected the changes in membrane permeability.[101] Furthermore, the spheres also seemed to enhance signals stemming from the cells directly, as the spectra contained features that indicated changes in membrane composition (CH_2 and CH_3 stretching modes), chromatin condensation (DNA phosphate stretching modes), and protein secondary structure (amide I band), which were used to detect the onset of apoptosis in ultrasound-treated cells.

Besides using colloidal nanoparticles inside cells to collect SEIRA signals, cells have also been monitored by bringing them close to SEIRA substrates. Shvets and colleagues developed a multiresonant substrate containing two antennas with a vertical connector, with which they studied live cells.[30,102] This specific structure leads to a Fano resonance, which informs about refractive index changes, a short-wavelength plasmon (single antenna) at $2900\,\mathrm{cm}^{-1}$ that enhances lipid vibrations, and a long-wavelength plasmon (antenna and horizontal coupler) at $1600\,\mathrm{cm}^{-1}$ enhancing the amide I and amide II bands. In a first study, the metasurface was integrated into a microfluidic chamber, where the cells were captured through a dielectrophoretic capturing mechanism.[102] The refractive index change caused by the captured cells could thus be monitored through the Fano resonance, while simultaneously enhancing the amide I and amide II signals, at a rate corresponding to the coverage of the metasurface, thereby giving quantitative information about cell attachment.

A second study monitored cells directly cultured on the metasurface under different environmental stimuli.[30] As membrane integrity largely depends on the presence of cholesterol, the cholesterol depletion agent methyl-β-cyclodextrin (MβCD) induced the decomposition of the membrane, and led to cell detachment. The three resonances of the metasurface, combined with PCA analysis, permitted the separate observation of refractive index changes in the medium, caused by the adsorption of MβCD, subsequent removal of cholesterol from the membrane without cell detachment, and refractive index changes in conjunction with the decrease in protein and fat signals, associated with cell detachment in the final phase. In a control experiment with MβCD-chol (a fat enriching membrane cholesterol), only the initial changes in refractive index and fat content after injection were observed, with the signal stabilizing afterwards.

Cellular mechanisms may vary locally between cells, but also within a single cell, and resolving these local differences gives a clearer picture of cellular processes. Whereas SEIRA substrates have been used to image live cells,[30] these images suffer from poor resolution due to the long wavelength of IR light. An interesting development to push simultaneously the limit of detection and spatial resolution of IR microscopy is the integration of atomic force microscopy (AFM) with SEIRA. Although the subject has been excellently reviewed,[4,103] we highlight here the applications of so-called tip-enhanced AFM-IR for imaging. In short, the metal-coated AFM tip functions as an antenna with the incident IR light being polarized along the AFM tip axis, leading to electric field enhancement at the sample surface. The method has been introduced in 2014 by Belkin and colleagues and yielded images of molecular monolayer islands with a spatial resolution of 25 nm.[104] In the application to cell imaging, the method was employed to elucidate conformational changes of transmembrane proteins embedded in the cellular membrane,[105] thereby paving the way toward analysing the functional heterogeneity of cells with SEIRA.

4 Chemical Sensing

SEIRA-based chemical sensors have essentially the same requirements as their biological sensor counterparts; the plasmon resonance should enhance one or more molecular vibrations in the analytes, which must be brought close to the plasmonic substrate in a reliable manner. In chemical sensors, oftentimes the presence of trace amounts of a specific compound of interest in an aqueous or gaseous mixture is the target species. Hence, lowering the limit of detection of the sensor via a higher EF is paramount.[106] For example, a stacked structure with elevated cross-shaped gold anten-

nas on top of dielectric pedestals induced plasmonic hotspots on top and below the antennas.[107] The 1-octadecanethiol (ODT) analyte molecules covered the substrate homogeneously, but the signal from the molecules in the nanogap between the substrate and the antennas (Figure 9a, b) was enhanced most due to the plasmonic hotspot in that location. This led to an overall reflection difference SEIRA signal of 36%, which is significantly higher than usually reported reflection difference signals in SEIRA studies (up to 10%).[91] However, the more commonly used figure of merit, the EF, was not reported. A different approach integrated a qualitative SEIRA sensor for polyvinyl chloride (PVC) with a quantitative sensor based on refractive index changes observed via a Fano resonance of the plasmonic structure in the sensor.[25] A split ring resonator on top of a gold mirror and silica spacer, engineered to enhance the C−Cl vibrational frequency at $636\,cm^{-1}$, qualitatively informed about the presence of PVC through its SEIRA spectral features. Additionally, a Fano resonance arose between the structure and the analyte molecules, sensitive to refractive index changes caused by the amount of PVC in the sample and thus informing about the PVC concentration, down to 0.5%. To lower the limit of detection of environmental sensors, devices have been designed to extract molecules from the environment, guiding, and concentrating them towards the sensor via specific analyte capture mechanisms.

4.1 Analyte Capture on SEIRA Substrates

Various strategies have been proposed to increase the affinity of targeted analyte molecules for plasmonic substrates. One of the most effective techniques involves surrounding the SEIRA substrate with a chemically-active matrix, which would trap the corresponding analyte molecules close to the substrate. Ideally, such matrices also aid in concentrating the analyte next to those regions with the largest near-field enhancements at the antennas, so that the signal is maximized.

This way of concentrating the analyte is especially useful in sensing of gas molecules because environmental toxins are often toxic at low concentrations. Gas sensing is critical to monitoring of environmental toxins, quality control of chemical processes, agricultural, and medical applications.[108] Industrial toxins such as carbon monoxide (CO), carbon dioxide (CO2) and volatile-organic compounds (VOCs) such as benzene, pose a major threat to human health and the environment.[109] To achieve an optimal sensing response, considering the sensitivity and selectivity of the sensor, one has to engineer the surface properties of the sensor material according to the targeted application.[110] An example of gas sensor utilizing SEIRA comprised a zeolite matrix to capture and condense benzene around gold nanoantennas, which were engineered to enhance the benzene band at $1480\,cm^{-1}$.[26] Through continuous collection and concentration of benzene in air, the sensor could detect 25 ppb of benzene within 10 minutes. In the same vein, gold nanoparticle arrays covered by a layer of a metal-organic framework (MOF) on a silicon nitride substrate, sensed carbon dioxide in air.[27] The MOF not only absorbed and concentrated ambient CO_2 molecules, but also delocalized the plasmonic enhancement over the whole sensor via

coupling of surface plasmon polaritons at the gold-silicon nitride and the gold-MOF interfaces. This means that the sensor did not rely on the enhancement at hotspots, but the CO_2 signal was enhanced throughout the whole sensor, with an EF of 1800.

We turn now to analyte determination on SEIRA substrates for aqueous samples. A different analyte concentration mechanism has been developed for aqueous samples. A hydrogel embedded with a chemical gradient on top of a SEIRA substrate was shown to draw analyte molecules from solution through the chemical gradient, towards the surface of the substrate, which led to a total signal increase of 10^2 compared to ATR measurements without chemical gradient.[111] The chemical gradient increased the signal by a factor of 15 after 17 hours of incubation. In addition to the signal enhancement due to the chemical gradient, the SEIRA EF due to the plasmonic substrate was 6.6, which compared with other studies reaching SEIRA EFs of up to 10^5, the SEIRA EF in this sensor could probably be improved in future iterations of the sensor. In another example, a liquid analyte was guided towards the plasmonic surface by means of a capillary flow.[112] The capillary effect was achieved by a hydrophilic SiO_2 mask surrounding the plasmonic substrate, which drew liquid towards the antenna array. The sensor was used to measure ethanol content in water, by enhancing the water IR absorption band at $1666\,cm^{-1}$. The sensor design focused more on the capillary-flow mechanisms than on lowering the limit of detection, as the water content in the mixture was varied between 0% and 100%, with 25% increments. An alternative approach toward enhancing the IR signal comprised concentrating the analytes, not just close to the substrate but directly on the plasmonic hotspots. In this particular example, aluminium ribbons on a gold film functioned as the plasmonic antennas. The aluminium ribbons sat on top of thinner germanium ribbons, which formed vertical nanoslits between the gold substrate and the aluminium ribbons, leading to plasmonic hotspots in the nanoslits (Figure 9c).[113] By dropcasting and evaporating the solvent on top of the ribbons, analyte molecules were condensed in the gap, i.e., the hotspots. The device was successful in trapping the molecules D-glucose and L-proline, and detecting them down to an amount of 1 pg on the sensor.

4.2 Multiresonant SEIRA Chemical Sensors

Multiband or broadband plasmonic substrates are of particular interest because they can be used to enhance multiple vibrational bands simultaneously. This might be applied to either enhance multiple vibrational bands of the same analyte,[114–116] or of different analytes.[31] The effect can either be achieved by broadband plasmonic substrates or substrates which display distinct, separated plasmon resonances. An example of a broadband plasmonic substrate was prepared by combining differently sized hook-shaped antennas into so-called supercells.[114] Such isolated hook-shaped antennas provide individually specific resonances that depend on their dimensions. If multiple arrays of different hook sizes are excited simultaneously, the plasmon response becomes broadband. In the supercell arrangement, each array contains a multitude of hook sizes. This supercell arrangement
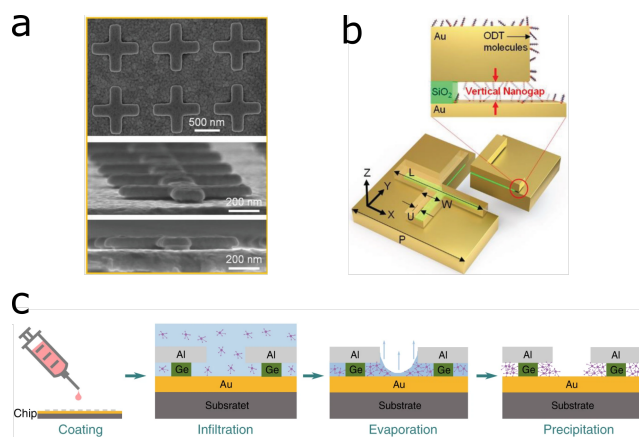
sizes, respectively.

Fig. 9 (a) SEM images of lifted cross-shaped gold antennas suspended on dielectric spacers, on top of a gold film forming a nanogap. (b) Lifted cross-shaped gold antennas suspended on dielectric spacers on top of a gold film with attached ODT molecules. Reprinted under the Creative Commons Attribution Licence (CC BY-NC 4.0) from ref. 107 with permission from John Wiley and Sons Publishing. (c) Aluminium ribbons on top of thinner germanium ribbons on a gold film form nanoslits, which can be used to trap analyte molecules through dropcasting the solution and evaporating the solvent. Reproduced under the Creative Commons License (CC BY 4.0) from ref. 113 with permission from Springer Nature.
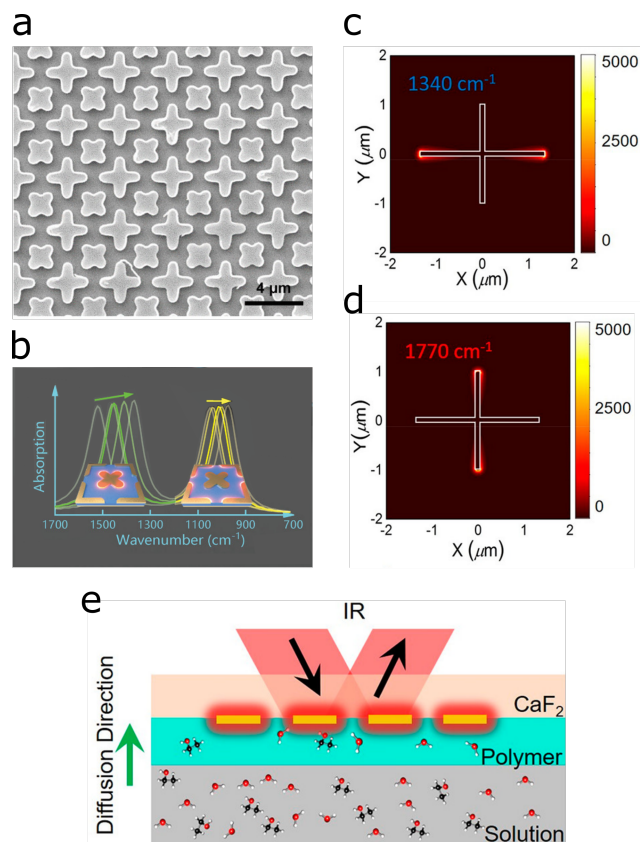
Fig. 10 (a) SEM images of crossed dual band perfect metamaterial absorber based on rotated crosses of different sizes. (b) Plasmonic response with two plasmonic peaks of the dual cross structure for simultaneous enhancement of the C=O and the C−O−C vibrational bands in poly(ethyl cyanoacrylate). Reproduced under the Creative Commons License (CC BY 4.0) from ref. 116 with permission from John Wiley and Sons Publishing. (c) Calculated resonance wavelength at $1340\,cm^{-1}$ corresponding to excitation of the long cross arm. (d) Calculated resonance wavelength at $1770\,cm^{-1}$ corresponding to excitation of the short cross arm. (e) Setup for measuring the diffusion constant of analytes with sugar. The SEIRA signal is measured at the plasmonic hotspots at the end of the antenna. The signal increase as a function of time informs about the diffusion constant of the analyte through the gel matrix. (not too scale). Adapted with permission from ref. 31. Copyright 2021 American Chemical Society.

yielded a more intense, combined broad resonance, allowing for detection of PMMA and silk with ten-fold higher plasmon intensity than a single antenna-size array. The design is also promising for future applications where multiple plasmon bands are required in close vicinity, as was demonstrated by the simultaneous enhancement of three acetone bands ($5.8\,\mu m$, $7.0\,\mu m$, and $7.3\,\mu m$).

An interesting development comprises the use of symmetric cross-shaped antennas, as they provide polarization-independent plasmon resonances, whereas asymmetric cross-shaped antennas can be tuned to different plasmon wavelengths for different polarizations.[31,115,116] For example, crossed-shaped nanoantennas for SEIRA enhancement with unpolarized light probed the SEIRA resonant effect and refractive index change upon PMMA binding. The SEIRA sensor achieved an enhancement of the PMMA signals with an EF of 4.8×10^4 (detection of 0.7 fmol of immobilized molecules).[115] In addition, PMMA binding was monitored via the shift of the centre wavelength of the plasmon resonance, induced by changes of the refractive index upon binding according to Equation 1. More details on plasmonic sensing based on refractive index changes can be found in other reviews.[117,118] A similar cross-shaped antenna with two equal-armed crosses of different sizes provide polarization-independent plasmons at two different wavelengths.[116]

The differently sized gold crosses were arranged at an angle of 45 degree to each other, and supported plasmonic peaks of quasi-equal intensity, which enhanced the C=O (at $1747.5\,cm^{-1}$) and the C−O−C vibrations (at $1252.8\,cm^{-1}$) of poly-ethyl cyanoacrylate (Figure 10a, b). The substrate was a metamaterial perfect absorber (see Section 5.2 below), which was used to probe thickness and chemical changes during the processing steps of poly-ethyl cyanoacrylate, with EFs of 449 and 334 for the both antenna

A different approach yielding two different resonances with crossed antennas is to engineer a cross with two different arm lengths[31]. Excited with unpolarized light, the cross-shaped antennas cover the spectral region from $1000\,cm^{-1}$ to $1700\,cm^{-1}$ (Figure 10c, d), which served for simultaneously monitoring two diffusing sugar species. The SEIRA substrate was surrounded by a gel matrix adjacent to the liquid containing the analytes. As the analytes diffuse through the gel, the concentration of analyte close to the antennas increases as does the SEIRA signal, which only probes the region close to the surface, informing about the diffusion constant (Figure 10e). The diffusion constant (time) of various sugar types was determined (glucose, maltose and maltotriose) and thereby the type of sugar and its concentration in a soft drink was evaluated. In a simplified study, solely one an-

tenna length and an adaptive data processing algorithm revealed the concentration of two sugar species (glucose and fructose) in water, down to $10\,\mathrm{g\,L^{-1}}$.[119]

Taken together, these studies render SEIRA a suitable sensing technique for gaseous and aqueous analytes with up to two chemical species measured at the same time via multiresonant substrates.

5 Advanced Multiresonant Substrates

SEIRA sensors should support LSPR modes at the energies of the molecular vibrations to be analysed. Therefore, design of substrates with multiple LSPR wavelengths would open the door to extracting information about multiple analytes in the sample. Some successful examples have been reported on the preparation of substrates, with resonances spanning wide frequency ranges in the mid-IR,[120,121] even extending into the near-IR.[54] Further efforts toward the combination of SEIRA and SERS additionally require plasmon resonances matching both the IR vibrational frequency and the Raman excitation laser. Therefore, lessons from engineering substrates with multiple IR resonances could be translated into the development of combined SEIRA and SERS substrates. In this section we review multiresonant substrates that have been used for SEIRA, and continue in Section 6 with combined substrates for SEIRA and SERS.

5.1 Rod-Antenna Multiresonant Substrates

Altug and colleagues combined nanoantennas of four different lengths into one substrate to provide four plasmon resonances spanning from the near-IR to the mid-IR (Figure 11).[54] Each antenna size had half the size of the larger antenna, resulting in doubling of the resonance frequency. To compensate for the decrease in resonance strength of higher frequency resonances, each number of consecutive antennas is increased by a factor of four resulting in plasmonic peaks of equal intensity. Additionally, by varying each of the antenna lengths, the corresponding resonance could be individually tuned by up to $60\,\%$ making the substrate more tailorable for specific applications. The platform was used for SEIRA and refractometry of PMMA and PS-PBd-PSin using the mid-IR peaks (f1, f2, f3) and near-IR peak (f4), respectively. As introduced in Section 3.3 above, a reduced design with two antenna sizes was used to observe IR signals of lipid membrane processes.[32]

Introducing more complex antenna-shapes, a Jerusalem cross-shaped nanoslit in a gold film acted as a dual-band resonator.[122] The geometry allows tuning of four different parameters, the length, the width of the arm, and the width of the tip in each arm, to alter the plasmon frequency as illustrated in Figure 12a-d. Another slit-design, formed by gold evaporated onto and next to SiO_2 bars, simultaneously leads to formation of a nanobar on top of the SiO_2, a nanoslit at the bottom of the SiO_2 and a vertical nanogap between the nanobar and the nanoslit.[123] Two resonance peaks appear for perpendicular and parallel illumination, whose resonance frequency is affected by the nanogap height and bar/slits size (bar and slit size are co-dependent).

Another structure allowing for independent changing of dimen-
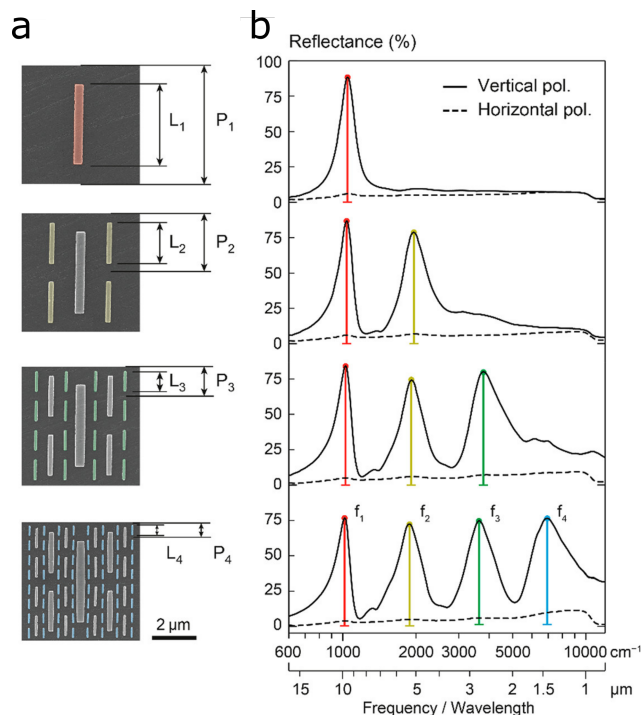

Fig. 11 (a) Superimposed multiresonant nanoantenna arrays with each additional antenna having half the length L and period P of the previous array, while the number get quadrupled. (b) Each nanoantenna size provides an additional specific resonance frequency corresponding to the antenna length (f1 to f4). Reprinted with permission from ref. 54. Copyright 2018 American Chemical Society.
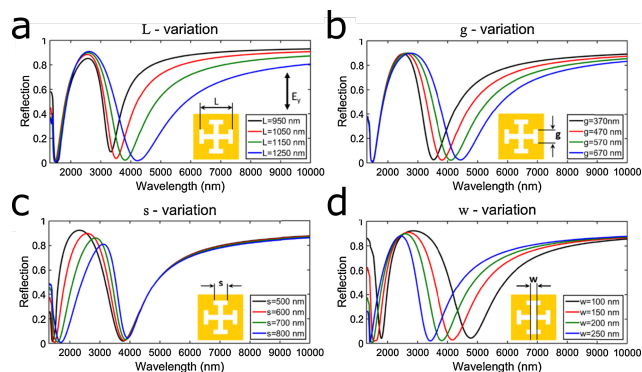

Fig. 12 (a-d) Dual-band plasmonic response of Jerusalem cross nanoslits. The windows show the different plasmonic responses upon altering the four different geometrical parameters: (a) the length of the arm L, (b, c) width of the individual tips g and s, and (d) the width of the arm w. Reprinted from ref. 50 with permission from Elsevier.

sions to control the plasmon resonance was the combination of a gold rod-nanoantenna and two split-ring resonators .[124] The nanorod functions as a bright coupler, whereas the split-ring resonator is a dark coupler. Depending on the polarization, the incident light excites either one or two arms of the split-ring resonator. If two arms are excited, the fundamental resonance mode is dark, and an additional bright resonance appears at a shorter wavelength. By independently changing the dimensions of the antenna, split-ring resonators, the spacing between those two, and the light's angle of incidence the plasmon resonance response of the structure was controlled, which led to a SEIRA signal enhancement of 10^4 for PMMA.

To conclude this section, more complex geometries, such as crosses or combinations of elements, offer multiple plasmon resonance through the individual elements but also the cross-talk between elements. Such structures furthermore offer multiple parameters to tune specific aspects of the plasmon resonance.

5.2 Plasmonic Perfect Absorbers

The metamaterial plasmonic structure (usually gold-based) of perfect plasmonic absorbers sits on top of a dielectric spacer and a gold mirror to reduce reflections and increase absorption.[120,125–127] The mirror-spacer combination enables the formation of a current loop between the opposite (excited) charges in the metamaterial above, leading to formation of a magnetic field in the dielectric spacer. By tuning the parameters of the layers, the impedance of the perfect absorber can be matched to that of free space, hence eliminating reflections.[67,120,125]

The design proposed by Durmaz et al., consists of a nanobar on top of a U-shaped split-ring resonator shown in Figure 13a. The U-shaped antenna contributes two plasmonic peaks, stemming from the top and side length, and the length of the nanobar leads to a third resonance (Figure 13b). Varying the height and width of the U-shaped antenna, as well as the length and width of the nanobar, individually fine-tunes the frequency of the respective peaks. The SEIRA capability for monitoring protein bilayers and polymer films was shown theoretically.[120] Along similar lines, a design supporting two resonances by lengthwise offset antennas of two different lengths, has been proposed.[125] The long and short antennas were engineered to enhance the SEIRA signal of C=O (1755 cm^{-1}) and C−H (2945 to 2985 cm^{-1}) peaks of a 10 nm-thick PMMA film.

A more involved design based on two mirrored asymmetric H antennas (Figure 13c) generates three plasmon peaks in parallel polarization and two plasmon peaks in perpendicular polarization, through formation of different dipole modes between the elements (Figure 13d).[126] The SEIRA compatibility was measured with a PMMA film. Introducing yet another multiresonant perfect absorber, the split cross (the central part of the cross is missing) leads to two sharp (high quality factor) resonances and a broader one (low quality factor).[127] The width, length, thickness of the antenna, the gap (split) size, and the period of the structure determined the resonance wavelengths. The antenna was used for refractive index sensing by monitoring the spectral peak shift. However, the design also has SEIRA potential because the
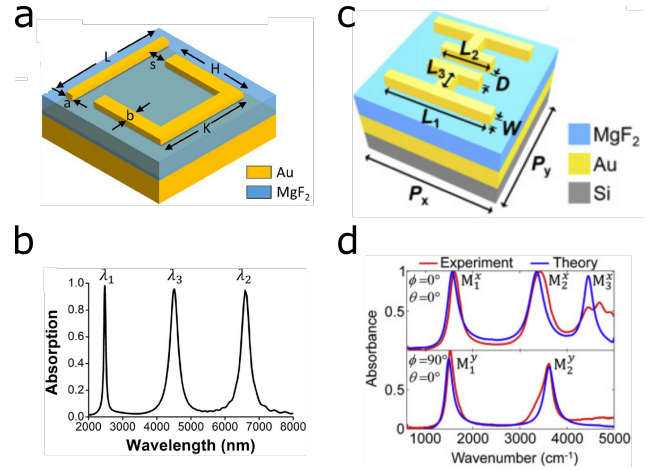

Fig. 13 Multi- and dual-band perfect absorbers based on gold nanostructures. The designs are constructed on gold mirrors and MgF$_2$ dielectric spacers. (a) Geometry of the nanobar and U-shaped antenna design. (b) Plasmonic response of the structure a, with λ_1, λ_2 and λ_3 corresponding to H, L and K, respectively. Reprinted from ref. 120 with permission from Elsevier. (c) Multi-band perfect absorber based on a mirrored asymmetric double H. (d) (TOP) Parallel illumination plasmonic response of structure e, with λ_1, λ_2 and λ_3 corresponding long and short antennas, and the space between these two, respectively. (BOTTOM) In perpendicular polarization the modes arise from dipolar and quadrupolar coupling between the two mirrored asymmetric H-shapes. Reprinted from ref. 126 with permission from Elsevier.

resonances lie in the mid-IR range, between 2500 nm and 3250 nm.

Kormaz et al. introduced a narrowband perfect absorber substrate, which due to the sharp peaks was particularly suited to exactly match the plasmon resonance to the molecular vibration.[128] The chair-like structure composed of multiple gold antennas of different lengths tuned to the absorption bands of PMMA detected the molecular fingerprints of a 10 nm thick PMMA layer. Overall, perfect-plasmonic-absorber-based SEIRA substrates offer plasmon resonances with exceptionally strong and sharp plasmon peaks.

5.3 Cayley Trees

Fractal plasmonics are plasmon resonances which occur in fractals, structures which are self-similar at different scales.[129] Recent advances in fractal plasmonics were reviewed by Wallace and Lagugné-Labarthet. We provide here a summary of selected findings for SEIRA applications.[129]

Cayley tree structures are nanoantennas radially arranged into hierarchical complexes, leading to interactions of the near- and far-field plasmon resonances that result in new plasmonic peaks. The application of such tree structures as plasmonic substrates was first introduced by Halas and co-workers.[130] Each branching event of the Y-shaped antennas is defined as the order of the structure and determines the number of peaks.[129,130] By varying the length of the rod length the resonance frequency may be shifted (Figure 14b). In addition, the authors found that individually varying the lengths of the antennas, the respective resonances shifted with little change to other resonances.[130]

Building on these findings, Wallace et al. developed dendritic structures of different orders spanning the near-IR and mid-IR re-

gion (1000 to 6000 cm^{-1}.[121] Higher orders of the structure add plasmonic peaks at lower energy (1000 cm^{-1}, 10 µm) and additionally shift the energy of the higher energy peaks to lower energies, as seen in Figure 14a.[121,131] In proof-of-principle SEIRA measurements with 4-NTP functionalized onto the dendritic fractals, the SEIRA enhancement was larger than for 4-NTP functionalized onto flat gold. In summary, combination of multiple plasmonic structures on a substrate may lead to multiple resonances with possible additional plasmonic effects through the interaction of the structure. These effects might be exploited to address an increasing number of molecular vibrations through SEIRA.
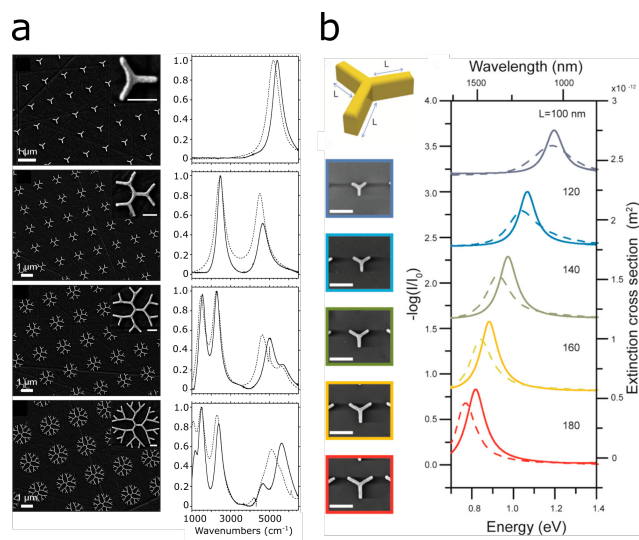

Fig. 14 Multiresonant plasmonic fractal structures. (a) SEM images of dendritic plasmonic structures of different orders (left) and corresponding normalized absorbance (right). Reprinted with permission from ref. 121. Copyright 2017 American Chemical Society. (b) Varying the resonance wavelength of first order Cayley trees by increasing the fundamental antenna length. Reprinted with permission from ref. 130. Copyright 2015 American Chemical Society.

6   SEIRA and SERS

Because IR and Raman spectroscopies rely on different selection rules, their combination provides a more complete picture of chemical composition and biological mechanisms.[132–135] To make use of the synergistic information the combination of IR and Raman offers at lower concentrations, the surface-enhancing substrate should support both SEIRA and SERS. As a general requirement, a combined SEIRA and SERS substrate should support plasmons, both at the energy of the molecular vibrations and matching the Raman excitation laser wavelength. For the latter, 785 nm lasers are most common, in particular for biological applications, but also UV, visible or 1064 nm lines are employed.

The achievable EF of SERS in inherently larger than that of SEIRA due to the different mechanisms behind the two techniques. In SERS, the incident and scattered photons are enhanced by the LSPR,[33–35] thus oftentimes attomolar concentrations may be detected.[136] On the other hand, SEIRA stems from a one-photon process and EFs are lower, with detected concentrations reaching the femtomolar range and rarely attomolar con-

centrations.[20,80,106] In SERS, particular substrate–analyte combinations may lead to improved enhancement, in comparison with other combinations.[136,137] To the best of our knowledge a similar selectivity of SEIRA substrates (unless the substrate is functionalized to achieve selectivity) has not been reported. However, SEIRA substrates can be engineered to enhance certain molecular vibrations over others because the plasmon resonance energy needs to overlap with that of the molecular vibration. Overall, the production of structures with electron-beam lithography, as usually employed in SEIRA, is highly reproducible and the identical methodology can be used for antennas of different sizes and shapes.[55,138] Widely reported issues in SERS are the closely related saturation and memory effects of substrates. Memory effects are related to saturation of the substrate surface by analyte molecules, so that other molecules are hindered from accessing it. Similarly, when monitoring samples over time, previously adsorbed molecules may prevent the detection of new ones derived from changes in the sample.[139] The dynamic observation of lipid membranes and cells on SEIRA substrates hints that for SEIRA this effect could be reduced,[30,55,69] but further investigation is required for confirmation of this assumption.

Attempts to combine surface enhancement for IR and Raman were made as early as 2001, based on evaporated gold films (Figure 15a).[140] The evaporation system leads to a rough surface structure of the gold film, which provided surface enhancement at various wavelengths, enabling SEIRA and SERS detection. Similarly, silver nanoparticles of various sizes prepared through wet-chemical methods on an Si substrate, provided SEIRA and SERS enhancement (Figure 15b),[141] as did self-assembled arrays of gold nanoparticles.[44] A similar substrate using silver nanoparticles was recently used in a more elaborate experiment, for the identification of bacterial species based on SEIRA and SERS (see Section 3.4).[99] Given the morphology-dependent plasmonic response of gold nanoparticles, deposition of tailored nanoparticles on a solid substrate appears as a suitable approach toward combined SEIRA and SERS. Although this idea has been demonstrated with gold nanostars functionalized onto silicon chips (Figure . 15c), the authors did not elaborate on the mechanism by which nanostars on top of the silicon chip were able to provide both SEIRA and SERS enhancement.[43]

On an interesting development, the structures of rough metallic surfaces were improved for use with SEIRA and SERS, by evaporating silver off-center, thus introducing an asymmetry that led to different silver layer coverage, and resulted in different layer thickness.[40] In this manner, thinner silver layer regions supported plasmons for SERS and thicker regions plasmons for SEIRA, as illustrated by Figure 16a-d. In the study, mercaptobenzonitrile (MBN) was chosen as a model analyte that shows molecular vibrations unique to SEIRA and SERS, as well as shared peaks, as displayed in Figure 16e-g. The enhancement factors for SEIRA and SERS were 170 and 10^4, respectively, with corresponding limits of detection of 0.17 and 0.012 monolayers. Overall, assemblies of nanoparticles, either obtained through evaporation of metals onto substrates or by deposition of synthesized nanoparticles, lead to resonances at multiple wavelengths, due to coupling of plasmonic modes supported by structures at different length
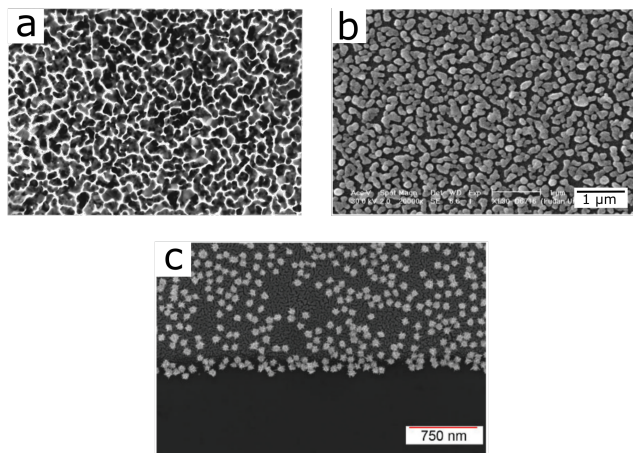
Fig. 15 (a) Evaporated gold film (magnification 150 000) used for SEIRA and SERS. Reprinted with permission from ref. 140. Copyright 2001 American Chemical Society. (b) Silver nanoparticles on top of a Si substrate. Reproduced from ref. 141 with permission from John Wiley and Sons Publishing. (c) Gold nanostars on silicon for SEIRA and SERS. Reproduced from ref. 43 with permission from the Royal Society of Chemistry.

scales. The similarity of the surface morphologies of evaporated metal and assembled nanoparticles are exemplified in Figure 15. Interestingly, the overall structure of evaporated and otherwise deposited metal films resemble each other visually, and lead to a similar plasmonic response. However, no studies have been reported to systematically compare their plasmonic response and enhancing efficiency.
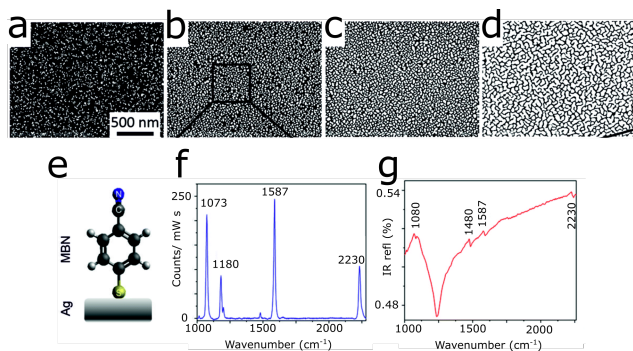

Fig. 16 (a-d) Growth of a silver (white) film on top of an Si (black) substrate by the gradient evaporation technique. (e) Chemical structure of MBN, here represented on top of a silver film. (f) SERS and (g) SEIRA spectra of MBN on gradient silver films. Reproduced from ref. 40 with permission from the Royal Society of Chemistry.

Moving now to deliberately-designed nanostructures for combined SEIRA and SERS, we show an example of hexagonally closed packed arrays of gold nanoshells (Figure 17a).[142] A NIR peak used for Raman enhancement stemmed from isolated nanoshells (dashed line in Figure 17b), whereas both the near- and mid-IR resonances result from the interaction and hybridization of plasmons from the nanoshells in the lattice of the array (solid curve in Figure 17b), which was confirmed by simulations.[39] The EF of the structure was reported to lie between 10^8 and 10^9 for SERS, and 10^4 for SEIRA. The platform was later used

by the same group to study SEIRA and SERS spectra of adsorbed adenine and adenosine monophosphate,[143] which revealed the orientation of the compound's ring with respect to the gold surface, by probing the difference in the vibrational mode caused by absorption onto the surface with respect to spectra of non-absorbed molecules.
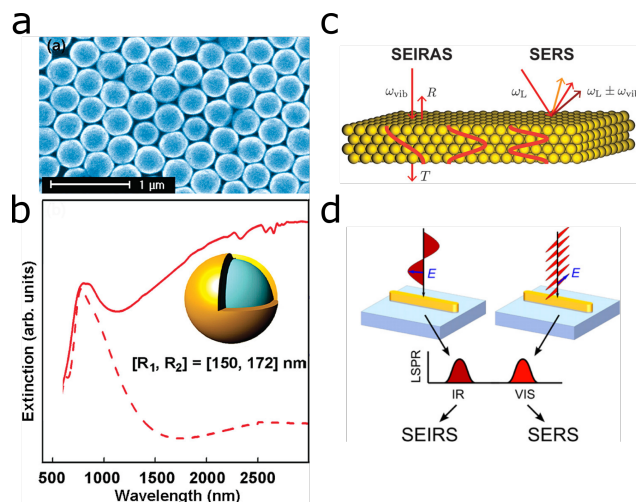

Fig. 17 (a-b) Arrays of Au nanoshells used as combined SEIRA and SERS substrates. (a) SEM image of a hexagonally closed packed monolayer of Au nanoshells. (b) Extinction spectra of nanoshell arrays (solid line) and isolated nanoshells (dashed line). Reprinted with permission from ref. 39. Copyright 2008 American Chemical Society. (c) Plasmonic crystals made from stacked gold spheres forming polaritonic standing waves at various wavelengths, for SEIRA and SERS. Reprinted with permission from ref. 38. Copyright 2021 American Chemical Society. (d) Gold nanoantennas used to simultaneously excite visible plasmons in perpendicular polarization (width of antenna) and IR plasmons with parallel polarization (length of antenna). Reprinted with permission from ref. 41. Copyright 2013 American Chemical Society.

Not only monolayers of gold shells, but also multilayered crystals made form gold spheres were shown to provide SEIRA and SERS enhancement stemming from the effect of the bulk arrangement.[38] The plasmonic crystals, made from gold spheres functionalized with polystyrene ligand molecules (which were also used to probe the enhancement), provided plasmonic hotspots between the spheres, but also plasmon polariton modes stemming from the bulk thickness of the film. These polaritonic resonances form standing waves in the 3D supercrystals at multiple wavelengths, depending on the integer number of multiples of the wavelengths fitting into the film, corresponding to the height of the crystal (Figure 17c). The plasmon polaritons are delocalized over the whole crystal, leading to uniform enhancement throughout the crystal with enhancement factors of 100 for SERS and 4 for SEIRA. In addition to this overall enhancement, in the hotspots between the spheres the EFs were 10^5 and 150, for SERS and SEIRA, respectively.

One of the most established SEIRA substrates comprises gold or silver rod-nanoantenna arrays fabricated on top of a substrate.[12] The antenna length is linearly related to the plasmon resonance and the polarization of the laser must be parallel to the antenna length, to excite this longitudinal plasmon mode. If the width

of the antenna corresponds to the plasmon wavelength needed for SERS, the same antenna can also provide SERS enhancement under perpendicular polarization of the laser, as schematically shown in Figure 17d. [41] The principle was tested with antennas of different lengths but the same width, thereby displaying the same Raman-excited plasmon. The system achieved a SEIRA EF of 6×10^5 and SERS EF of 10^3. While not mentioned in the paper, in our view the lower EF for SERS can be at least in part explained by the lower plasmon intensity of the lower wavelength transversal plasmon mode, which has a lower resonance intensity by approximately a factor of seven than the longitudinal mode resonance of the longest antenna.

Finally, we would like to highlight two reports on the measurement of surface-enhanced IR, Raman and fluorescence signal, using the same substrate. Log-periodic nanoantennas lead to plasmon resonances across a wide frequency range, which can be explored for combination of SERS and SEIRA. [144] The circular arrangement of three log-periodic antennas provided polarization-independent plasmons with fundamental resonances at 1176, 1721, and 2504 nm, as well as plasmons extending into the visible range (Figure 18a, b). [45] The design, using an excitation wavelength of 640 nm, would enhance the fluorescent Alexa Fluor 647 signal by a factor of 4.8. On the same substrate, the SEIRA and SERS signals of streptadivin were measured with EFs of 1×10^4 and 1.2×10^4, respectively.

Similarly, a fractal pattern consisting of superimposed nanoprisms generated multiple resonances in the near- and mid-IR, leading to SEIRA, SERS and surface-enhanced fluorescence (SEF). [145] The pattern shown in Figure 18d, composed of hexagonally arranged large (1 to $2\,\mu m$) and small ($0.25\,\mu m$), prisms was fabricated by two consecutive rounds of nanosphere lithography. The arrangement of small prisms generates two plasmonic peaks, a dipolar mode at 950 nm and a multipolar mode at 640 nm. The larger prisms with side lengths of $1\,\mu m$ caused resonances in the mid-IR at approximately $3000\,cm^{-1}$. By tuning the size of the prisms, the resonance could be tailored to the analyte as illustrated by Figure 18c. The potential of the structure for SERS, SEIRA and SEF was demonstrated with 4-nitrothiophenol with EFs of 10^3 for SEIRA and 10^5 for SERS.

Despite the ability of SERS to reach theoretically higher enhancement factors than SEIRA, in combined studies the EF of SEIRA was reported as being higher [41,140,145] or of equal magnitude [45] as the SERS enhancement, which we attribute to the optimization of the SEIRA factor. With further design options we see both of these EFs increase within the same substrate.

7 Conclusions redand Outlook

Surface-enhanced infrared spectroscopy has evolved into a promising sensing method for biological and chemical samples. Metallic antennas provide plasmon resonances in the IR for the enhancement of molecular vibrations. An important aspect hereby involves matching the plasmon resonance wavelength to the molecular vibration via the antenna geometry. With this requisite in mind, the detection and analysis of biomolecules, such as protein secondary structure, DNA, and lipids, have been enabled. By tuning the plasmon resonances to the amide I absorption band,
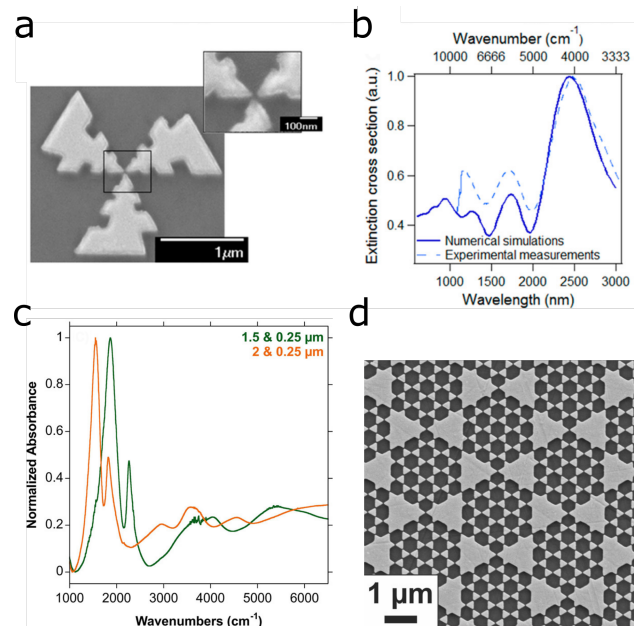

Fig. 18 (a) SEM image of three-arm log-periodic gold nanoantennas. (b) Simulated (solid line) and experimental (dashed line) Exctinction cross section of log-periodic gold nanoantennas. Reprinted with permission from ref. 45. Copyright 2013 American Chemical Society. (c) Absorbance of multiresonant plasmonic superimposed prism arrays. The plasmonic response curves changes when show varying the size of the larger prism, from $1.5\,\mu m$ (green) to $2.0\,\mu m$ (orange). (d) SEM image of superimposed prism array with small prism size of $0.25\,\mu m$ and large prism size of $1.25\,\mu m$. Adapted with permission from ref. 145. Copyright 2016 American Chemical Society.

changes in the protein secondary structure could be observed. Detection of DNA sequences has also been demonstrated, including identification of a single point mutation through the corresponding spectral features. Regarding chemical sensing, surface functionalization is typically required, in combination with antennas of optimized plasmon resonance, to provide capture mechanisms that allow e.g. detection in the gas phase (benzene, carbon dioxide).

The development of substrates with multiple resonances in the IR additionally allows for simultaneous monitoring of multiple biological molecules, such as proteins, lipids and carbohydrates. Especially the combination of such multiresonant substrates with advanced data analysis methods (such as multiple linear regression, PCA and machine learning) resulted in SEIRA-based sensing platforms for monitoring multiple biological constituents in lipid bilayers and cells cultured on top of SEIRA substrates. The applications of such multiresonant SEIRA sensors has also been extended into the analysis of chemicals, with promising application in quality control of products.

Multiresonant substrates also open up the possibility of integrating SEIRA detection with SERS sensing on the same substrate, given that the available plasmon resonances provide enhancement of both IR absorption and Raman scattering. In some cases, the substrate may also provide surface-enhanced fluorescence in addition to SEIRA and SERS. Henceforth, future sensors have the possibility to provide a more complete picture of the

(bio-)chemical environment of a sample.

We propose that an important step forward in the engineering of SEIRA substrates is the production of cost-effective substrates, with no need for costly electron-beam lithography methods. Improved methods should allow the development faster, cheaper and more accessible possibilities for the production of SEIRA based sensors. Interesting advances have been made by means of direct laser writing photolithography,[146] and colloidal lithography.[147] A further step towards making SEIRA more accessible is the production of substrates via synthesis of mid-IR plasmonic particles, which would circumvent the use of expensive cleanrooms. SEIRA enhancement has already been demonstrated using colloidal silver nanorods.[148] Another example in this direction is the synthesis of rod-shaped gold/silver nanorattles with plasmonic resonance extendable up to the mid-IR.[149]

Finally, we should highlight the combination of multiple resonances in the same substrate to open the door to new sensing schemes for using IR light through more sensitive visible detectors. The upconversion of IR to visible light facilitated through dual-wavelength antennas may lead to a novel generation of infrared detectors.[150,151]

Author Contributions

M.W. wrote the draft and prepared the figures. A.S. revised the manuscript. L.M.L.-M. coordinated the preparation and revised the manuscript.

Conflicts of interest

There are no conflicts to declare.

Acknowledgements

Notes and references

1 P. J. Larkin, in *Infrared and Raman Spectroscopy (Second Edition)*, Elsevier, Amsterdam, 2nd edn, 2018, ch. 2, pp. 7–28.

2 B. H. Stuart, *Infrared Spectroscopy: Fundamentals and Applications*, Wiley, Chichester, 2005.

3 A. Pinczuk and E. Burstein, in *Light Scattering in Solids*, ed. M. Cardona, Springer, Berlin Heidelberg, 1975, ch. 2, pp. 23–78.

4 D. Kurouski, A. Dazzi, R. Zenobi and A. Centrone, *Chem. Soc. Rev.*, 2020, **49**, 3315–3347.

5 R. Adato and H. Altug, *Nat. Commun.*, 2013, **4**, 2154.

6 D. Bohm and D. Pines, *Phys. Rev.*, 1951, **82**, 625–634.

7 R. H. Ritchie, *Phys. Rev.*, 1957, **106**, 874–881.

8 S. A. Maier, *Plasmonics: Fundamentals and Applications*, Springer, New York, 2007.

9 M. Pelton, J. Aizpurua and G. Bryant, *Laser Photonics Rev.*, 2008, **2**, 136–159.

10 M. Durach, A. Rusina, M. I. Stockman and K. Nelson, *Nano Lett.*, 2007, **7**, 3145–3149.

11 S. Schlücker, *Angew. Chem. Int. Ed.*, 2014, **53**, 4756–4795.

12 F. Neubrech, C. Huck, K. Weber, A. Pucci and H. Giessen, *Chem. Rev.*, 2017, **117**, 5110–5145.

13 A. Hartstein, J. R. Kirtley and J. C. Tsang, *Phys. Rev. Lett.*, 1980, **45**, 201–204.

14 M. Fleischmann, P. J. Hendra and A. J. McQuillan, *Chem. Phys. Lett.*, 1974, **26**, 163–166.

15 D. L. Jeanmaire and R. P. Van Duyne, *J. Electroanal. Chem.*, 1977, **84**, 1–20.

16 M. G. Albrecht and J. A. Creighton, *J. Am. Chem. Soc.*, 1977, **99**, 5215–5217.

17 S. G. Schultz, M. Janik-Czachor and R. P. Van Duyne, *Surf. Sci.*, 1981, **104**, 419–434.

18 S. Nie and S. R. Emory, *Science*, 1997, **275**, 1102–1106.

19 K. Kneipp, Y. Wang, H. Kneipp, L. T. Perelman, I. Itzkan, R. R. Dasari and M. S. Feld, *Phys. Rev. Lett.*, 1997, **78**, 1667–1670.

20 V. Di Meo, M. Moccia, G. Sanità, A. Crescitelli, A. Lamberti, V. Galdi, I. Rendina and E. Esposito, *Front. Bioeng. Biotechnol.*, 2021, **9**, 666121.

21 L. Dong, X. Yang, C. Zhang, B. Cerjan, L. Zhou, M. L. Tseng, Y. Zhang, A. Alabastri, P. Nordlander and N. J. Halas, *Nano Lett.*, 2017, **17**, 5768–5774.

22 D. Ji, A. Cheney, N. Zhang, H. Song, J. Gao, X. Zeng, H. Hu, S. Jiang, Z. Yu and Q. Gan, *Adv. Opt. Mater.*, 2017, **5**, 1700223.

23 F. Neubrech, A. Pucci, T. W. Cornelius, S. Karim, A. García-Etxarri and J. Aizpurua, *Phys. Rev. Lett.*, 2008, **101**, 157403.

24 J. Vogt, C. Huck, F. Neubrech, A. Toma, D. Gerbert and A. Pucci, *Phys. Chem. Chem. Phys.*, 2015, **17**, 21169–21175.

25 C.-T. Lin, T.-J. Yen and T.-Y. Huang, *Coatings*, 2021, **11**, 789.

26 J. Nuñez, A. Boersma, J. Grand, S. Mintova and B. Sciacca, *Adv. Funct. Mater.*, 2021, **31**, 2101623.

27 X. Chong, Y. Zhang, E. Li, K.-J. Kim, P. R. Ohodnicki, C.-h. Chang and A. X. Wang, *ACS Sens.*, 2018, **3**, 230–238.

28 R. Semenyshyn, M. Hentschel, C. Huck, J. Vogt, F. Weiher, H. Giessen and F. Neubrech, *ACS Sens.*, 2019, **4**, 1966–1972.

29 A. F. S. Seiça, M. H. Iqbal, A. Carvalho, J.-y. Choe, F. Boulmedais and P. Hellwig, *ACS Sens.*, 2021, **6**, 2875–2882.

30 S. H. Huang, J. Li, Z. Fan, R. Delgado and G. Shvets, *Lab Chip*, 2021, **21**, 3991–4004.

31 H. Chen, G. Singhal, F. Neubrech, R. Liu, J. S. Katz, S. Matteucci, S. G. Arturo, D. Wasserman, H. Giessen and P. V. Braun, *ACS Nano*, 2021, **15**, 10393–10405.

32 D. Rodrigo, A. Tittl, N. Ait-Bouziad, A. John-Herpin, O. Limaj, C. Kelly, D. Yoo, N. J. Wittenberg, S.-H. Oh, H. A. Lashuel and H. Altug, *Nat. Commun.*, 2018, **9**, 2160.

33 A. D. McFarland, M. A. Young, J. A. Dieringer and R. P. Van Duyne, *J. Phys. Chem. B*, 2005, **109**, 11279–11285.

34 N. G. Greeneltch, M. G. Blaber, G. C. Schatz and R. P. Van Duyne, *J. Phys. Chem. C*, 2013, **117**, 2554–2558.

35 T. Itoh, K. Yoshida, V. Biju, Y. Kikkawa, M. Ishikawa and Y. Ozaki, *Phys. Rev. B*, 2007, **76**, 085405.

36 H.-L. Wang, E.-M. You, R. Panneerselvam, S.-Y. Ding and Z.-Q. Tian, *Light Sci. Appl.*, 2021, **10**, 161.

37 J. Nong, L. Tang, G. Lan, P. Luo, Z. Li, D. Huang, J. Shen and W. Wei, *Small*, 2021, **17**, 2004640.

38 N. S. Mueller, E. Pfitzner, Y. Okamura, G. Gordeev, P. Kusch, H. Lange, J. Heberle, F. Schulz and S. Reich, *ACS Nano*, 2021, **15**, 5523–5533.

39 F. Le, D. W. Brandl, Y. A. Urzhumov, H. Wang, J. Kundu, N. J. Halas, J. Aizpurua and P. Nordlander, *ACS Nano*, 2008, **2**, 707–718.

40 D. Gkogkou, T. Shaykhutdinov, C. Kratz, T. W. H. Oates, P. Hildebrandt, I. M. Weidinger, K. H. Ly, N. Esser and K. Hinrichs, *Analyst*, 2019, **144**, 5271–5276.

41 C. D'Andrea, J. Bochterle, A. Toma, C. Huck, F. Neubrech, E. Messina, B. Fazio, O. M. Maragò, E. Di Fabrizio, M. Lamy de La Chapelle, P. G. Gucciardi and A. Pucci, *ACS Nano*, 2013, **7**, 3522–3531.

42 A. Campu, F. Lerouge, D. Chateau, F. Chaput, P. Baldeck, S. Parola, D. Maniu, A. M. Craciun, A. Vulpoi, S. Astilean and M. Focsan, *Anal. Chem.*, 2018, **90**, 8567–8575.

43 O. Bibikova, J. Haas, A. I. López-Lorente, A. Popov, M. Kinnunen, I. Meglinski and B. Mizaikoff, *Analyst*, 2017, **142**, 951–958.

44 M. Baia, F. Toderas, L. Baia, D. Maniu and S. Astilean, *ChemPhysChem*, 2009, **10**, 1106–1111.

45 H. Aouani, M. Rahmani, H. Šípová, V. Torres, K. Hegnerová, M. Beruete, J. Homola, M. Hong, M. Navarro-Cía and S. A. Maier, *J. Phys. Chem. C*, 2013, **117**, 18620–18626.

46 F. Neubrech, T. Kolb, R. Lovrincic, G. Fahsold, A. Pucci, J. Aizpurua, T. W. Cornelius, M. E. Toimil-Molares, R. Neumann and S. Karim, *Appl. Phys. Lett.*, 2006, **89**, 253104.

47 F. Neubrech and A. Pucci, *IEEE J. Sel. Top. Quantum Electron.*, 2013, **19**, 4600809.

48 J. Aizpurua, G. W. Bryant, L. J. Richter, F. J. García de Abajo, B. K. Kelley and T. Mallouk, *Phys. Rev. B*, 2005, **71**, 235420.

49 L. Novotny, *Phys. Rev. Lett.*, 2007, **98**, 266802.

50 F. Neubrech, D. Weber, R. Lovrincic, A. Pucci, M. Lopes, T. Toury and M. L. de La Chapelle, *Appl. Phys. Lett.*, 2008, **93**, 163105.

51 T. Neuman, P. Alonso-González, A. Garcia-Etxarri, M. Schnell, R. Hillenbrand and J. Aizpurua, *Laser Photonics Rev.*, 2015, **9**, 637–649.

52 G. W. Bryant, F. J. García de Abajo and J. Aizpurua, *Nano Lett.*, 2008, **8**, 631–636.

53 T. Neuman, C. Huck, J. Vogt, F. Neubrech, R. Hillenbrand, J. Aizpurua and A. Pucci, *J. Phys. Chem. C*, 2015, **119**, 26652–26662.

54 D. Rodrigo, A. Tittl, A. John-Herpin, O. Limaj and H. Altug, *ACS Photonics*, 2018, **5**, 4903–4911.

55 A. John-Herpin, D. Kavungal, L. von Mücke and H. Altug, *Adv. Mater.*, 2021, **33**, 2006054.

56 J. Vogt, C. Huck, F. Neubrech and A. Pucci, in *Frontiers of Plasmon Enhanced Spectroscopy*, ed. Y. Ozaki, G. C. Schatz, D. Graham and T. Itoh, ACS Symposium Series 1246, American Chemical Society, Washington, DC, 2016, vol. 2, pp. 1–19.

57 R. Adato, A. A. Yanik, J. J. Amsden, D. L. Kaplan, F. G. Omenetto, M. K. Hong, S. Erramilli and H. Altug, *Proc. Natl. Acad. Sci. U. S. A.*, 2009, **106**, 19227–19232.

58 S. Bagheri, K. Weber, T. Gissibl, T. Weiss, F. Neubrech and H. Giessen, *ACS Photonics*, 2015, **2**, 779–786.

59 U. Fano, *Phys. Rev.*, 1961, **124**, 1866–1878.

60 A. E. Miroshnichenko, S. Flach and Y. S. Kivshar, *Rev. Mod. Phys.*, 2010, **82**, 2257–2298.

61 Y. S. Joe, A. M. Satanin and C. S. Kim, *Phys. Scr.*, 2006, **74**, 259–266.

62 B. Luk'yanchuk, N. I. Zheludev, S. A. Maier, N. J. Halas, P. Nordlander, H. Giessen and C. T. Chong, *Nat. Mater.*, 2010, **9**, 707–715.

63 R. Adato, S. Aksu and H. Altug, *Mater. Today*, 2015, **18**, 436–446.

64 R. Adato, A. Artar, S. Erramilli and H. Altug, *Nano Lett.*, 2013, **13**, 2584–2591.

65 S. Fan, W. Suh and J. D. Joannopoulos, *J. Opt. Soc. Am. A*, 2003, **20**, 569–572.

66 L. Verslegers, Z. Yu, P. B. Catrysse and S. Fan, *J. Opt. Soc. Am. B*, 2010, **27**, 1947–1956.

67 T. G. Mayerhöfer and J. Popp, *Nanophotonics*, 2018, **7**, 39–79.

68 I. M. Pryce, Y. A. Kelaita, K. Aydin and H. A. Atwater, *ACS Nano*, 2011, **5**, 8167–8174.

69 O. Limaj, D. Etezadi, N. J. Wittenberg, D. Rodrigo, D. Yoo, S.-H. Oh and H. Altug, *Nano Lett.*, 2016, **16**, 1502–1508.

70 X. Yang, Z. Sun, T. Low, H. Hu, X. Guo, F. J. García de Abajo, P. Avouris and Q. Dai, *Adv. Mater.*, 2018, **30**, 1704896.

71 D. Etezadi, J. B. Warner IV, F. S. Ruggeri, G. Dietler, H. A. Lashuel and H. Altug, *Light: Sci. Appl.*, 2017, **6**, e17029.

72 Y. Hu, Á. I. López-Lorente and B. Mizaikoff, *ACS Photonics*, 2019, **6**, 2182–2197.

73 S.-H. Oh, H. Altug, X. Jin, T. Low, S. J. Koester, A. P. Ivanov, J. B. Edel, P. Avouris and M. S. Strano, *Nat. Commun.*, 2021, **12**, 3824.

74 M. L. Tseng, Y. Jahani, A. Leitis and H. Altug, *ACS Photonics*, 2021, **8**, 47–60.

75 D. Rosas-Vara, J. R. Molina-Contreras, F. Villalobos-Piña, J. C. Zenteno, B. Buentello-Volante, O. F. Chacon-Camacho, R. Ayala-Ramírez, C. Frausto-Reyes, R. Hernández-Martínez and M. A. Ríos-Corripio, *Chem. Pap.*, 2020, **74**, 1079–1086.

76 Z. Yao, Q. Zhang, W. Zhu, M. Galluzzi, W. Zhou, J. Li, A. V. Zayats and X.-F. Yu, *Nanoscale*, 2021, **13**, 10133–10142.

77 A. M. Shrivastav, U. Cvelbar and I. Abdulhalim, *Commun. Biol.*, 2021, **4**, 70.

78 X. Hui, C. Yang, D. Li, X. He, H. Huang, H. Zhou, M. Chen, C. Lee and X. Mu, *Adv. Sci.*, 2021, **8**, 2100583.

79 V. Di Meo, A. Crescitelli, M. Moccia, A. Sandomenico, A. M. Cusano, M. Portaccio, M. Lepore, V. Galdi and E. Esposito, *Nanophotonics*, 2020, **9**, 3921–3930.

80 R. Semenyshyn, F. Mörz, T. Steinle, M. Ubl, M. Hentschel,

F. Neubrech and H. Giessen, *ACS Photonics*, 2019, **6**, 2636–2642.

81 F. U. Hartl, *Annu. Rev. Biochem*, 2017, **86**, 21–26.

82 A. Dong, P. Huang and W. S. Caughey, *Biochemistry*, 1990, **29**, 3303–3308.

83 R. Semenyshyn, M. Hentschel, C. Stanglmair, T. Teutsch, C. Tarin, C. Pacholski, H. Giessen and F. Neubrech, *Nano Lett.*, 2019, **19**, 1–7.

84 D. Etezadi, J. B. Warner IV, H. A. Lashuel and H. Altug, *ACS Sens.*, 2018, **3**, 1109–1117.

85 P. Zucchiatti, G. Birarda, A. Cerea, M. S. Semrau, A. Hubarevich, P. Storici, F. De Angelis, A. Toma and L. Vaccari, *Nanoscale*, 2021, **13**, 7667–7677.

86 C. Huck, F. Neubrech, J. Vogt, A. Toma, D. Gerbert, J. Katzmann, T. Härtling and A. Pucci, *ACS Nano*, 2014, **8**, 4908–4914.

87 A. John-Herpin, A. Tittl and H. Altug, *ACS Photonics*, 2018, **5**, 4117–4124.

88 V. Russo, N. Michieli, T. Cesca, C. Scian, D. Silvestri, M. Morpurgo and G. Mattei, *Nanoscale*, 2017, **9**, 10117–10125.

89 A. Campu, F. Lerouge, D. Maniu, K. Magyari and M. Focsan, *J. Mol. Struct.*, 2021, **1246**, 131160.

90 F. Omeis, A. F. Santos Seica, R. Bernard, N. Javahiraly, H. Majjad, D. Moss and P. Hellwig, *ACS Sens.*, 2020, **5**, 2191–2197.

91 C. Huck, J. Vogt, M. Sendner, D. Hengstler, F. Neubrech and A. Pucci, *ACS Photonics*, 2015, **2**, 1489–1497.

92 G. Armelles, A. Cebollada, D. G. Cava, J. Alvarez-Malmagro and M. Vélez, *Plasmonics*, 2021, **17**, 321–329.

93 P. Dumas, F. Polack, B. Lagarde, O. Chubar, J. Giorgetta and S. Lefrançois, *Infrared Phys. Technol.*, 2006, **49**, 152–160.

94 A. R. W. McKellar, *J. Mol. Spectrosc.*, 2010, **262**, 1–10.

95 L. M. Miller and R. J. Smith, *Vib. Spectrosc.*, 2005, **38**, 237–240.

96 R. Najmanovich, J. Kuttner, V. Sobolev and M. Edelman, *Proteins*, 2000, **39**, 261–268.

97 J. A. Allen, R. A. Halverson-Tamboli and M. M. Rasenick, *Nat. Rev. Neurosci.*, 2007, **8**, 128–140.

98 A. N. Dizaji, N. S. Ozek, A. Yilmaz, F. Aysin and M. Yilmaz, *Colloids Surf. B*, 2021, **206**, 111939.

99 H. Yilmaz, S. S. Mohapatra and M. Culha, *Spectrochim. Acta A*, 2022, **268**, 120699.

100 D. Li, H. Zhou, X. Hui, X. He and X. Mu, *Anal. Chem.*, 2021, **93**, 9437–9444.

101 F. Domenici, A. Capocefalo, F. Brasili, A. Bedini, C. Giliberti, R. Palomba, I. Silvestri, S. Scarpa, S. Morrone, G. Paradossi, M. D. Frogley and G. Cinque, *Sci. Rep.*, 2019, **9**, 11845.

102 G. Kelp, J. Li, J. Lu, N. DiNapoli, R. Delgado, C. Liu, D. Fan, S. Dutta-Gupta and G. Shvets, *Lab Chip*, 2020, **20**, 2136–2153.

103 A. Dazzi and C. B. Prater, *Chem. Rev.*, 2017, **117**, 5146–5173.

104 F. Lu, M. Jin and M. A. Belkin, *Nat. Photonics*, 2014, **8**, 307–312.

105 V. Giliberti, R. Polito, E. Ritter, M. Broser, P. Hegemann, L. Puskar, U. Schade, L. Zanetti-Polzi, I. Daidone, S. Corni, F. Rusconi, P. Biagioni, L. Baldassarre and M. Ortolani, *Nano Lett.*, 2019, **19**, 3104–3114.

106 H. Zhou, D. Li, X. Hui and X. Mu, *Int. J. Optomechatronics*, 2021, **15**, 97–119.

107 I. Hwang, M. Kim, J. Yu, J. Lee, J.-H. Choi, S. A. Park, W. S. Chang, J. Lee and J.-Y. Jung, *Small Methods*, 2021, **5**, 2100277.

108 Y. Li, A.-S. Xiao, B. Zou, H.-X. Zhang, K.-L. Yan and Y. Lin, *Polyhedron*, 2018, **154**, 83–97.

109 J. M. Walker, S. A. Akbar and P. A. Morris, *Sens. Actuators B Chem.*, 2019, **286**, 624–640.

110 M. Drobek, J.-H. Kim, M. Bechelany, C. Vallicari, A. Julbe and S. S. Kim, *ACS Appl. Mater. Interfaces*, 2016, **8**, 8323–8328.

111 H. Chen, S. Zhang, K. A. Miller and P. V. Braun, *ACS Appl. Polym. Mater.*, 2020, **2**, 3929–3935.

112 K. Shih, Z. Ren, C. Wang and C. Lee, *J. Phys. D: Appl. Phys.*, 2019, **52**, 394001.

113 X. Miao, L. Yan, Y. Wu and P. Q. Liu, *Light Sci. Appl.*, 2021, **10**, 5.

114 Z. Ren, J. Wei, D. Hasan, B. Dong, G. Zhou and C. Lee, *2019 20th International Conference on Solid-State Sensors, Actuators and Microsystems & Eurosensors XXXIII (TRANSDUCERS & EUROSENSORS XXXIII)*, Berlin, 2019.

115 V. Di Meo, A. Caporale, A. Crescitelli, M. Janneh, E. Palange, A. De Marcellis, M. Portaccio, M. Lepore, I. Rendina, M. Ruvo and E. Esposito, *Sens. Actuators B Chem.*, 2019, **286**, 600–607.

116 D. Li, H. Zhou, X. Hui, X. He, H. Huang, J. Zhang, X. Mu, C. Lee and Y. Yang, *Adv. Sci.*, 2021, **8**, 2101879.

117 S. Balbinot, A. M. Srivastav, J. Vidic, I. Abdulhalim and M. Manzano, *Trends Food Sci. Technol.*, 2021, **111**, 128–140.

118 J. R. Mejía-Salazar and O. N. Oliveira, *Chem. Rev.*, 2018, **118**, 10617–10625.

119 B. Schuler, L. Kühner, M. Hentschel, H. Giessen and C. Tarín, *Sensors*, 2019, **19**, 3053.

120 H. Durmaz, Y. Li and A. E. Cetin, *Sens. Actuators B Chem.*, 2018, **275**, 174–179.

121 G. Q. Wallace, H. C. Foy, S. M. Rosendahl and F. Lagugné-Labarthet, *J. Phys. Chem. C*, 2017, **121**, 9497–9507.

122 A. E. Cetin, S. Kaya, A. Mertiri, E. Aslan, S. Erramilli, H. Altug and M. Turkmen, *Photonics Nanostructures: Fundam. Appl.*, 2015, **15**, 73–80.

123 X. Chen, C. Wang, Y. Yao and C. Wang, *ACS Nano*, 2017, **11**, 8034–8046.

124 Z. Ren, Z. Dang and C. Lee, *2020 IEEE 33rd International Conference on Micro Electro Mechanical Systems (MEMS)*, Vancouver, 2020.

125 A. E. Cetin, S. Korkmaz, H. Durmaz, E. Aslan, S. Kaya, R. Paiella and M. Turkmen, *Adv. Opt. Mater.*, 2016, **4**, 1274–1280.

126 E. Aslan, E. Aslan, M. Turkmen and O. G. Saracoglu, *Opt.*

Mater., 2017, **73**, 213–222.

127 A. Yang, K. Yang, L. Zhou, J. Li, X. Tan, H. Liu, H. Song, J. Tang, F. Liu and F. Yi, *Opt. Commun.*, 2017, **387**, 55–60.

128 S. Korkmaz, M. Turkmen and S. Aksu, *Sens. Actuator A Phys.*, 2020, **301**, 111757.

129 G. Q. Wallace and F. Lagugné-Labarthet, *Analyst*, 2019, **144**, 13–30.

130 S. Gottheim, H. Zhang, A. O. Govorov and N. J. Halas, *ACS Nano*, 2015, **9**, 3284–3292.

131 G. Q. Wallace, D. M. McRae and F. Lagugné-Labarthet, *Opt. Lett.*, 2019, **44**, 3865–3868.

132 K. Kochan, H. Peng, B. R. Wood and V. S. Haritos, *Biotechnol. Biofuels*, 2018, **11**, 106.

133 X. Li, D. Zhang, Y. Bai, W. Wang, J. Liang and J.-X. Cheng, *Anal. Chem.*, 2019, **91**, 10750–10756.

134 J. Nallala, O. Piot, M.-D. Diebold, C. Gobinet, O. Bouché, M. Manfait and G. D. Sockalingum, *Appl. Spectrosc.*, 2014, **68**, 57–68.

135 D. Perez-Guaita, K. Kochan, M. Martin, D. W. Andrew, P. Heraud, J. S. Richards and B. R. Wood, *Vib. Spectrosc.*, 2017, **91**, 46–58.

136 J. Langer, D. Jimenez de Aberasturi, J. Aizpurua, R. A. Alvarez-Puebla, B. Auguié, J. J. Baumberg, G. C. Bazan, S. E. J. Bell, A. Boisen, A. G. Brolo, J. Choo, D. Cialla-May, V. Deckert, L. Fabris, K. Faulds, F. J. García de Abajo, R. Goodacre, D. Graham, A. J. Haes, C. L. Haynes, C. Huck, T. Itoh, M. Käll, J. Kneipp, N. A. Kotov, H. Kuang, E. C. Le Ru, H. K. Lee, J.-F. Li, X. Y. Ling, S. A. Maier, T. Mayerhöfer, M. Moskovits, K. Murakoshi, J.-M. Nam, S. Nie, Y. Ozaki, I. Pastoriza-Santos, J. Perez-Juste, J. Popp, A. Pucci, S. Reich, B. Ren, G. C. Schatz, T. Shegai, S. Schlücker, L.-L. Tay, K. G. Thomas, Z.-Q. Tian, R. P. Van Duyne, T. Vo-Dinh, Y. Wang, K. A. Willets, C. Xu, H. Xu, Y. Xu, Y. S. Yamamoto, B. Zhao and L. M. Liz-Marzán, *ACS Nano*, 2020, **14**, 28–117.

137 J. Reguera, J. Langer, D. Jiménez de Aberasturi and L. M.

Liz-Marzán, *Chem. Soc. Rev.*, 2017, **46**, 3866–3885.

138 S. E. J. Bell, G. Charron, E. Cortés, J. Kneipp, M. L. Chapelle, J. Langer, M. Procházka, V. Tran and S. Schlücker, *Angew. Chem. Int. Ed.*, 2020, **59**, 5454–5462.

139 J. Plou, M. Charconnet, I. García, J. Calvo and L. M. Liz-Marzán, *ACS Nano*, 2021, **15**, 8984–8995.

140 S. Sánchez-Cortés, C. Domingo, J. V. García-Ramos and J. A. Aznárez, *Langmuir*, 2001, **17**, 1157–1162.

141 B.-B. Huang, J.-Y. Wang, S.-J. Huo and W.-B. Cai, *Surf. Interface Anal.*, 2008, **40**, 81–84.

142 H. Wang, J. Kundu and N. J. Halas, *Angew. Chem. Int. Ed.*, 2007, **46**, 9040–9044.

143 J. Kundu, O. Neumann, B. G. Janesko, D. Zhang, S. Lal, A. Barhoumi, G. E. Scuseria and N. J. Halas, *J. Phys. Chem. C*, 2009, **113**, 14390–14397.

144 H. Aouani, H. Šípová, M. Rahmani, M. Navarro-Cia, K. Hegnerová, J. Homola, M. Hong and S. A. Maier, *ACS Nano*, 2013, **7**, 669–675.

145 G. Q. Wallace, M. Tabatabaei, R. Hou, M. J. Coady, P. R. Norton, T. S. Simpson, S. M. Rosendahl, A. Merlen and F. Lagugné-Labarthet, *ACS Photonics*, 2016, **3**, 1723–1732.

146 A. Braun and S. A. Maier, *ACS Sens.*, 2016, **1**, 1155–1162.

147 K. Chen, T. Duy Dao and T. Nagao, *Sci. Rep.*, 2017, **7**, 44069.

148 N. Li, H. Yin, X. Zhuo, B. Yang, X.-M. Zhu and J. Wang, *Adv. Opt. Mater.*, 2018, **6**, 1800436.

149 S. Rodal-Cedeira, presented in part at IX Iberian Meeting on Colloids and Interfaces (RICI IX), Santiago de Compostela, July, 2022.

150 W. Chen, P. Roelli, H. Hu, S. Verlekar, S. P. Amirtharaj, A. I. Barreda, T. J. Kippenberg, M. Kovylina, E. Verhagen, A. Martínez and C. Galland, *Science*, 2021, **374**, 1264–1267.

151 A. Xomalis, X. Zheng, R. Chikkaraddy, Z. Koczor, E. Miele, E. Rosta, G. A. E. Vandenbosch, A. Martínez and J. J. Baumberg, *Science*, 2021, **374**, 1268–1271.